J. Fluid Mech. (2024), *vol.* 985, A11, doi:10.1017/jfm.2024.287

Langmuir turbulence in suspended kelp farms

Tong Bo[1],†, **James C. McWilliams**[1], **Chao Yan**[2] **and Marcelo Chamecki**[1]

[1]Department of Atmospheric and Oceanic Sciences, University of California Los Angeles, Los Angeles, CA 90095-1565, USA

[2]Institute of Urban Meteorology, China Meteorological Administration, Beijing 100089, PR China

(Received 10 October 2023; revised 15 February 2024; accepted 18 March 2024)

This study investigates the influence of suspended kelp farms on ocean mixed layer hydrodynamics in the presence of currents and waves. We use the large eddy simulation method, where the wave effect is incorporated by solving the wave-averaged equations. Distinct Langmuir circulation patterns are generated within various suspended farm configurations, including horizontally uniform kelp blocks and spaced kelp rows. Intensified turbulence arises from the farm-generated Langmuir circulation, as opposed to the standard Langmuir turbulence observed without a farm. The creation of Langmuir circulation within the farm is attributed to two primary factors depending on farm configuration: (i) enhanced vertical shear due to kelp frond area density variability, and (ii) enhanced lateral shear due to canopy discontinuity at lateral edges of spaced rows. Both enhanced vertical and lateral shear of streamwise velocity, representing the lateral and vertical vorticity components, respectively, can be tilted into downstream vorticity to create Langmuir circulation. This vorticity tilting is driven by the Craik–Leibovich vortex force associated with the Stokes drift of surface gravity waves. In addition to the farm-generated Langmuir turbulence, canopy shear layer turbulence is created at the farm bottom edge due to drag discontinuity. The intensity of different types of turbulence depends on both kelp frond area density and the geometric configuration of the farm. The farm-generated turbulence has substantial consequences for nutrient supply and kelp growth. These findings also underscore the significance of the presence of obstacle structures in modifying ocean mixed layer characteristics.

Key words: ocean processes, turbulent boundary layers

† Email address for correspondence: tbo@atmos.ucla.edu

© The Author(s), 2024. Published by Cambridge University Press. This is an Open Access article, distributed under the terms of the Creative Commons Attribution licence (http://creativecommons.org/licenses/by/4.0), which permits unrestricted re-use, distribution and reproduction, provided the original article is properly cited.

1. Introduction

Marine macroalgae, such as kelp, provide essential habitats, shelter and food sources for a diverse range of marine species, with immense importance for biodiversity preservation and ecosystem health (e.g. Dayton 1985; Teagle *et al.* 2017). The cultivation and harvest of macroalgae also has the potential to become a sustainable strategy for biofuel production, food supply and carbon sequestration (Ghadiryanfar *et al.* 2016; Ferdouse *et al.* 2018). Given the constraints posed by the ecological carrying capacity of existing near-shore aquaculture, recent interest has thus arisen in expanding macroalgal farming offshore (Troell *et al.* 2009; Yan, McWilliams & Chamecki 2021; Frieder *et al.* 2022). These offshore macroalgal farms are usually attached to suspended structures near the ocean surface, typically within the ocean mixed layer (OML).

An essential factor affecting the performance of suspended macroalgal farms is their interaction with the hydrodynamic processes in the OML (Yan *et al.* 2021; Frieder *et al.* 2022). Kelp exerts a drag force on the flow (e.g. Thom 1971; Jackson 1997), resulting in attenuation in current velocity and wave motions (Rosman *et al.* 2007; Monismith *et al.* 2022). Discontinuities in drag can also lead to the development of shear layers and eddies at the boundaries of the canopy (Plew 2011), which may cause significant modifications in OML turbulence (Yan *et al.* 2021). These altered hydrodynamic conditions due to the presence of kelp can determine nutrient availability, chemical transport and salinity and temperature conditions in the farms, thereby affecting kelp growth.

Moreover, the variability of farm configurations, e.g. farm geometry and orientation with respect to currents and waves, can introduce added complexity into the interaction between kelp farms and OML turbulence. In addition, kelp growth and harvesting can effectively alter the frond surface area density (Frieder *et al.* 2022), consequently influencing the drag force and canopy flow profiles. A comprehensive understanding of the complex hydrodynamic processes in the OML with the presence of suspended farms is therefore crucial for optimally designing farm configurations and tactically managing harvesting practices.

The investigation of suspended farm hydrodynamics, beyond its direct implications for farm performance, also contributes to our broader understanding of how obstacle structures modify the OML. Various obstacle structures located near the ocean surface boundary, e.g. aquatic vegetation, engineered offshore platforms, ships, buoys and sea ice, have the potential to influence the hydrodynamic interactions among winds, waves and currents. These modifications to OML hydrodynamics may consequently result in alterations to other OML characteristics, e.g. heat transport and salinity mixing.

Suspended kelp farms, hydrodynamically classified as suspended canopies, share similarities with submerged canopies that are located on the bottom boundary (Plew 2011; Tseung, Kikkert & Plew 2016). The emergence of shear layer turbulence at the top of the canopy has received considerable attention in the context of submerged canopy flow (e.g. Finnigan 2000; Nepf 2012). Likewise, for a suspended canopy, a shear layer can develop at the bottom of the canopy, leading to generation of turbulence and the exchange of momentum and scalars between the canopy and the underlying flow (Plew 2011). Additionally, for suspended canopies of finite dimensions, an adjustment region typically develops within the canopy starting from the leading edge (Tseung *et al.* 2016), where the flow adapts to the drag imposed by the canopy, similar to that of finite-length submerged canopies (Belcher, Jerram & Hunt 2003; Rominger & Nepf 2011). Subsequent to this adjustment region, a fully developed canopy flow region emerges, followed by a wake region downstream from the canopy. While the suspended canopy in general behaves like an inverted submerged canopy (Plew 2011), distinct hydrodynamic conditions can arise, as a result of the different boundary conditions at the surface and the prevalent presence of surface gravity waves in the OML.

A prominent turbulent process in the OML is the Langmuir circulation driven by wind and waves (e.g. Leibovich 1983; McWilliams, Sullivan & Moeng 1997; Thorpe 2004). It is typically visible on the ocean surface as streaks of foam or debris, i.e. surface convergence lines, and is usually roughly parallel to the directions of wind and waves (Langmuir 1938). The generation of Langmuir circulation depends critically on the interaction between the sheared wind-driven current and the Stokes drift of surface gravity waves (e.g. Craik & Leibovich 1976; Craik 1977; Leibovich 1977). Vorticity tilting due to the vertically sheared Stokes drift can cause instability to generate coherent Langmuir cell structures aligned with the downwind direction, and this is known as the Craik–Leibovich (CL) 2 mechanism. The intensified turbulence associated with Langmuir circulation can enhance the vertical transport and mixing in the upper ocean (McWilliams *et al.* 1997; McWilliams & Sullivan 2000) and could even be important for producing and maintaining the uniform OML (Li & Garrett 1997; Thorpe 2004).

Nevertheless, the interplay between Langmuir turbulence and aquatic vegetation remains largely unexplored. The significance of Langmuir circulation extends beyond hydrodynamics, also playing a crucial role in biogeochemical transport in the OML and influencing the distribution of macroalgae (Evans & Taylor 1980; Dierssen *et al.* 2009; Qiao *et al.* 2009). On the other hand, the presence of vegetation can modify wind-driven currents and waves in the OML, and is thus expected to affect the generation of Langmuir turbulence. Yan *et al.* (2021) investigated the creation of attached Langmuir circulation in a suspended macroalgal farm with a specific configuration, where spaced rows of kelp are aligned parallel to the flow and waves. In addition to the generation of canopy shear layer turbulence below the farm, Langmuir-type turbulence was found to occur within the farm, with a stronger magnitude than the standard Langmuir turbulence generated without a farm. These various types of farm-generated turbulence can significantly affect nutrient transport in the OML, potentially leading to feedback on farm performance. Therefore, a more comprehensive examination of the physical mechanisms behind turbulence generation by suspended farms, e.g. the interaction between the Stokes drift and farm-modulated ocean currents, is necessary for an improved understanding of OML hydrodynamics. The dependence of canopy flow properties on different farm configurations also merits further investigation, as a crucial aspect of offshore farm planning and nutrient management.

In this study, we employ large eddy simulation (LES) to understand the influence of suspended kelp farms on OML hydrodynamics, with a particular focus on the mechanisms of turbulence generation. We also explore how varying farm configurations and frond density distributions affect these turbulence generation mechanisms. Section 2 describes the numerical method and the various farm configurations investigated in this study. Section 3 presents the statistics of mean flow, secondary flow and turbulence in the farm. In particular, we focus on three representative farm configurations to highlight the various flow patterns arising from different horizontal arrangements and vertical frond density profiles. Section 4 examines the energy budget to understand sources of farm-generated turbulence. Section 5 investigates the vorticity dynamics in the farm to illustrate the generation mechanisms of Langmuir circulations. In § 6, we explore other farm parameters that affect turbulence generation, including the effective frond area density, farm orientation and farm length. Section 7 presents the conclusion.

2. Methods

2.1. *Model description*

We use LES to investigate turbulence generation associated with suspended kelp farms. Large eddy simulation is a widely used tool in studying OML turbulence and more detailed discussion can be found in Chamecki *et al.* (2019). The code used in this study has been validated against Langmuir turbulence simulations in McWilliams *et al.* (1997) and applied to previous research in the macroalgal farm and boundary layer flow (Yan *et al.* 2021; Yan, McWilliams & Chamecki 2022). The present LES framework is based on the wave-averaged and grid-filtered equations for mass, momentum and heat

$$\nabla \cdot \tilde{\boldsymbol{u}} = 0, \tag{2.1}$$

$$\frac{\partial \tilde{\boldsymbol{u}}}{\partial t} + \tilde{\boldsymbol{u}} \cdot \nabla \tilde{\boldsymbol{u}} = -\nabla \varPi - f\boldsymbol{e}_z \times \left(\tilde{\boldsymbol{u}} + \boldsymbol{u}_s - \boldsymbol{u}_g\right) + \boldsymbol{u}_s \times \tilde{\boldsymbol{\zeta}} + \left(1 - \frac{\tilde{\rho}}{\rho_0}\right) g\boldsymbol{e}_z - \nabla \cdot \boldsymbol{\tau}^d - \boldsymbol{F}_D, \tag{2.2}$$

$$\frac{\partial \tilde{\theta}}{\partial t} + (\tilde{\boldsymbol{u}} + \boldsymbol{u}_s) \cdot \nabla \tilde{\theta} = -\nabla \cdot \boldsymbol{\pi}_\theta. \tag{2.3}$$

This mathematical model was initially introduced in McWilliams *et al.* (1997) by extending the original CL equations (Craik & Leibovich 1976), with the effects of planetary rotation and advection of scalars by Stokes drift incorporated.

The tilde in (2.1), (2.2) and (2.3) represents the grid-filtered variables. In the Cartesian coordinate system $\boldsymbol{x} = (x, y, z)$, the velocity vector is $\tilde{\boldsymbol{u}} = (\tilde{u}, \tilde{v}, \tilde{w})$, i.e. the streamwise, lateral (cross-stream) and vertical components, respectively. In (2.2), $\varPi$ is the modified pressure (e.g. Chamecki *et al.* 2019), f is the Coriolis frequency, g is the gravitational acceleration, $\boldsymbol{e}_z$ is the unit vector in the vertical direction and $\tilde{\boldsymbol{\zeta}} = \nabla \times \tilde{\boldsymbol{u}}$ is the filtered vorticity. Here, $\boldsymbol{u}_s$ is the Stokes drift associated with surface gravity waves, and $\boldsymbol{u}_g$ is a geostrophic current that represents the effect of mesoscale ocean flows. The geostrophic current is driven by an external pressure gradient $f\boldsymbol{e}_z \times \boldsymbol{u}_g$. The term $\boldsymbol{F}_D$ represents the drag force imposed by the canopy onto the flow, and the detailed treatment of canopy drag will be described later.

In (2.2), $\tilde{\rho}$ is the filtered density, and ρ_0 is the reference density. We assume that variations in density are only caused by the potential temperature $\tilde{\theta}$ via a linear relationship $\rho = \rho_0[1 - \alpha(\theta - \theta_0)]$, where $\alpha = 2 \times 10^{-4}\ \mathrm{K}^{-1}$ is the thermal expansion coefficient and θ_0 is the reference potential temperature corresponding to ρ_0. The term $\boldsymbol{\tau}^d$ is the deviatoric part of the subgrid-scale (SGS) stress tensor $\boldsymbol{\tau} = \widetilde{\boldsymbol{u}\boldsymbol{u}} - \tilde{\boldsymbol{u}}\,\tilde{\boldsymbol{u}}$, and $\boldsymbol{\pi}_\theta = \widetilde{\boldsymbol{u}\theta} - \tilde{\boldsymbol{u}}\,\tilde{\theta}$ is the SGS heat flux. The SGS stress is modelled using the Lagrangian scale-dependent dynamic Smagorinsky model (Bou-Zeid, Meneveau & Parlange 2005). The SGS heat flux is modelled using an eddy diffusivity closure, with diffusivity obtained from SGS viscosity and a prescribed value of turbulent Prandtl number $Pr_t = 0.4$. Molecular viscosity and diffusivity are assumed to be negligible for the high Reynolds number flows examined in this study.

The surface waves are not explicitly resolved in the model, and the time-averaged influences of waves are incorporated by imposing the Stokes drift $\boldsymbol{u}_s$. We consider a simple case of monochromatic deep water wave propagating in the x direction, with amplitude a_w and frequency $\omega = \sqrt{gk}$, where k is the wavenumber. The Stokes drift velocity thus reduces to $\boldsymbol{u}_s = (u_s, 0, 0)$, and

$$u_s = U_s \mathrm{e}^{2kz}, \tag{2.4}$$

where $U_s = \omega k a_w^2$ is the Stokes drift velocity at the surface. The effect of waves on OML turbulence is represented by the CL vortex force $\boldsymbol{u}_s \times \tilde{\boldsymbol{\zeta}} = (0, -u_s\tilde{\zeta}_z, u_s\tilde{\zeta}_y)$, i.e. the third term on the right-hand side of (2.2). While the presence of the canopy may additionally influence waves, Stokes drift and the wave–current interaction (e.g. Luhar *et al.* 2010, 2013; Rosman *et al.* 2013), these effects are estimated to be reasonably small for the macroalgal farm simulations considered here and thus have been neglected (Yan *et al.* 2021).

The parameterization of the canopy drag force F_D in (2.2) is expressed as (Shaw & Schumann 1992; Pan, Chamecki & Isard 2014; Yan *et al.* 2021)

$$\boldsymbol{F}_D = \tfrac{1}{2} C_D a \boldsymbol{P} \boldsymbol{\cdot} (|\tilde{\boldsymbol{u}}|\tilde{\boldsymbol{u}}) . \tag{2.5}$$

Here, C_D is the drag coefficient, and $|\tilde{\boldsymbol{u}}|$ is the magnitude of the filtered velocity. Henceforth, for simplicity we will drop the tilde symbols that denote grid-filtered variables. We use $C_D = 0.0148$ based on the experimental study of Utter & Denny (1996), and more detailed discussion on this choice of C_D can be found in Yan *et al.* (2021). In (2.5), a is the frond surface area density (or foliage area density, area per volume, m^{-1}). The frond surface area of macroalgae is obtained by conversion of the algal biomass (Frieder *et al.* 2022). Rather than directly resolving the geometry of the macroalgae fronds and stipes, their overall drag on the flow is characterized through this quadratic formula in the model, with a representative frond area density a for each grid cell. The coefficient tensor $\boldsymbol{P}$ stands for the projection of frond surface area into each direction, and in the present study we use $\boldsymbol{P} = \frac{1}{2}\boldsymbol{I}$, where $\boldsymbol{I}$ is the identity matrix (Yan *et al.* 2021).

In the realistic farm set-up, macroalgae are attached to subsurface structures at the bottom of the canopy (Charrier, Wichard & Reddy 2018; Yan *et al.* 2021), and buoyancy typically keeps them upright in the water column (e.g. Koehl & Wainwright 1977). We therefore assume macroalgae fronds and stipes to maintain an approximately fixed position in the flow, except for exhibiting small-amplitude oscillations passively following the wave orbital motion. This assumption is supported by the analyses in Yan *et al.* (2021), which examined a set of dimensionless parameters including the Cauchy number and buoyancy number. It is also consistent with the omission of the wave orbital velocity in (2.5), neglecting the interaction between wave and canopy drag (Yan *et al.* 2021; McWilliams 2023). A more detailed description of macroalgal farm configurations will be presented in § 2.3.

The present LES framework resolves the flow and temperature fields using a grid structure with horizontally collocated points and a vertically staggered arrangement. A pseudospectral method is used in the horizontal direction, and vertical derivatives are discretized with a second-order central finite-difference method. Aliasing errors arising from the nonlinear terms are removed through padding on the basis of the 3/2 rule. The equations are advanced in time using the fully explicit second-order Adams–Bashforth scheme.

2.2. *Simulation set-up*

The present study aims to investigate the mechanisms of turbulence generation in the OML in the presence of suspended kelp farms, with a focus on examining various farm configurations and frond area density distributions. Therefore, instead of considering a range of oceanic factors like wind stress, waves, currents and mixed layer depth, we only select one set of representative oceanic conditions. The simulation parameters used here are generally the same as those in McWilliams *et al.* (1997). The flow is driven by a constant wind stress $\tau_w = 0.037\,\mathrm{N\,m^{-2}}$ at the surface boundary, corresponding to a wind speed at 10 m height above the surface of $U_{10} = 5\,\mathrm{m\,s^{-1}}$ and a friction velocity of $u_* = 0.0061\,\mathrm{m\,s^{-1}}$. The deep water waves have an amplitude of $a_w = 0.8$ m, and the wavelength is $\lambda = 60$ m, corresponding to a wave period of 6.2 s. This leads to a surface Stokes velocity of $U_s = 0.068\,\mathrm{m\,s^{-1}}$ and a turbulent Langmuir number of $La_t = \sqrt{u_*/U_s} = 0.3$.

In addition to the wind-driven current, a geostrophic flow $\boldsymbol{u_g} = (u_g, 0, 0)$ is imposed in the x-direction, i.e. same as the direction of wind and waves. The geostrophic flow is driven by an external pressure gradient fu_g in the y-direction, with a constant value of $u_g = 0.2\,\mathrm{m\,s^{-1}}$, assuming that variations of mesoscale flow are small within the temporal and spatial scales relevant to the present study. The Coriolis frequency $f = 10^{-4}\,\mathrm{s^{-1}}$ corresponds to 45 °N latitude. The initial mixed layer depth of the upstream inflow is 25 m, and a stably stratified layer is beneath it, with a uniform temperature gradient $\mathrm{d}\theta/\mathrm{d}z = 0.01\,\mathrm{K\,m^{-1}}$ (buoyancy frequency $N = 0.0044\,\mathrm{s^{-1}}$). We assume no heat flux at the surface boundary.

Kelp farm simulations are conducted on a $L_x \times L_y \times L_z = 800 \times 208 \times 120\,\mathrm{m^3}$ domain, with $N_x \times N_y \times N_z = 400 \times 104 \times 240$ grid cells. The mesh is uniformly distributed, with a horizontal resolution of 2 m and a vertical resolution of 0.5 m. A sensitivity test on grid size was conducted in Yan *et al.* (2021), and doubling the resolution in all the three dimensions yielded consistent results. The simulations are run for 15 000 s to allow for the adjustment of the OML to the suspended canopy, and for another 9000 s after the fully developed turbulence state is reached to analyse turbulence statistics. A quasi-equilibrium state with converged turbulence statistics is established in the 9000 s period used for analysis, as examined in Yan *et al.* (2021).

The farm is located in the middle of the domain from $x = 0$ to $x = L_{MF}$, with a farm length of $L_{MF} = 400$ m (figure 1). The upstream boundary is at $x = -L_u = -150$ m, and the downstream boundary is at a distance of $L_d = 250$ m from the farm trailing edge. In the y-direction the farm extends across the entire domain with a periodic boundary, i.e. effectively assuming an infinite farm width to eliminate the complexities arising from the lateral farm edges. In the vertical direction the farm is between the sea surface and $h_b = 20$ m (the farm base), i.e. the depth at which the suspended structure is deployed. While most simulations are set as $L_x = 800$ m and $L_{MF} = 400$ m, an additional simulation is conducted with an extended domain length of $L_x = 1200$ m (and $N_x = 600$) and farm length of $L_{MF} = 800$ m to examine the effect of a longer farm. More detailed descriptions of farm parameters will be presented in § 2.3.

A precursor inflow method is used to simulate the spatially evolving flow in the kelp farm simulations (Churchfield *et al.* 2012; Stevens, Graham & Meneveau 2014; Yan *et al.* 2021). In this method the turbulent velocity and temperature fields at the upstream boundary of the domain are obtained from a precursor simulation. The precursor simulation is separately conducted with identical conditions without the farm, until the turbulent flow reaches a quasi-equilibrium state. A fringe region (length $L_{fr} = 100$ m) is used at the downstream end of the domain of the farm simulations. In this fringe region the flow field is smoothly forced toward the inflow conditions provided by the precursor simulation at the end of every time step. The precursor inflow method allows the turbulence produced by the precursor simulation to enter the domain of the farm simulations, while permitting the farm wakes to exit without cycling back through the periodic boundary conditions.

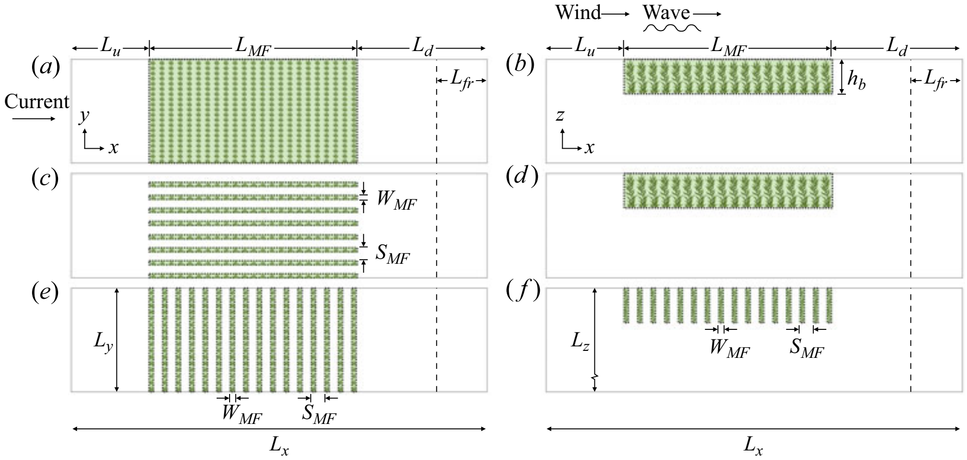

Figure 1. Model domain and three types of farm configurations. (*a*,*b*) The farm block configuration (top view and side view). (*c*,*d*) The configuration with kelp rows aligned with the current direction. (*e*,*f*) The configuration with kelp rows oriented perpendicular to the current direction.

2.3. *Farm configuration*

The cultivation of macroalgae in open ocean environments involves a diverse range of aquaculture structures. A representative farm configuration is considered here and consists of a series of organized longlines spaced horizontally (Yan *et al.* 2021; Frieder *et al.* 2022). Each longline is anchored at both ends and is also connected to surface buoys. Growth ropes, where kelp is seeded, are attached perpendicular to the longline. Kelp is cultivated at $h_b = 20$ m, i.e. the longline deployment depth, and grows upright due to its buoyancy. The frond surface area density is assumed to be horizontally uniform within each canopy row (each longline set) for simplicity. In the present study, we explore various farm configurations by varying the canopy row spacing and orientation and by comparing different vertical profiles of frond surface area density within the row.

Two vertical profiles of frond surface area density are considered, which represent two different growth stages of kelp (Frieder *et al.* 2022): (i) an intermediate growth stage with kelp extending from the farm base to around 2 m below the sea surface; (ii) a fully grown stage with kelp extending from the farm base to the sea surface, with notably high frond area density at the top due to a large portion of the fronds floating at the sea surface. The frond surface area density profiles of the two stages are obtained by conversion of the algal biomass (Frieder *et al.* 2022) and are plotted in figure 2. Harvest practices typically concentrate on the uppermost 1–2 m part of kelp, resulting in the reduction of frond density to zero near the surface. This causes the frond density profile to revert to the earlier growth stage from the fully grown stage. Henceforth, we refer to the earlier growth stage – with a low frond density near the surface – as the ‘harvested’ profile, and the fully grown stage – with a high frond density near the surface – is referred to as the ‘ripe’ profile.

In addition, we examine a variety of kelp row arrangements for each vertical profile of frond area density. The farm parameters for all the simulations are summarized in table 1 in Appendix A. The first set of arrangements (cases ‘S’) has the longlines aligned parallel to the x-direction (the direction of waves and geostrophic flow), extending the length of the farm. The longlines are repeated at a fixed distance S_{MF} in the y-direction (figure 1*c*,*d*). We conduct a range of farm simulations with varying S_{MF} and kelp row width (growth rope length) W_{MF} (details provided in Appendix A).

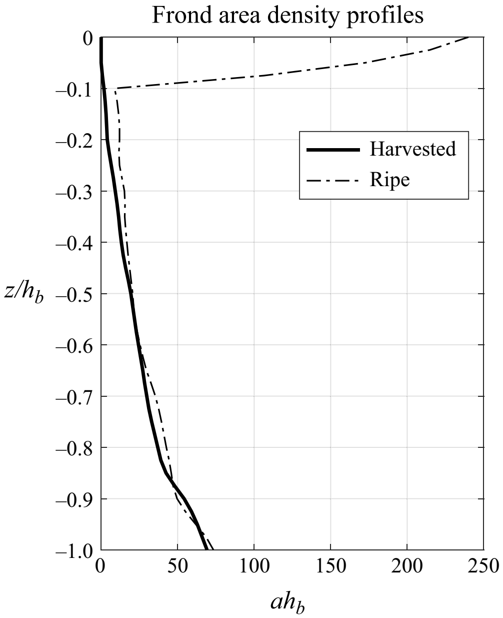

Figure 2. Vertical profiles of frond surface area density a, normalized by the farm base depth h_b. The solid line represents the harvested profile, and the dash-dotted line represents the ripe profile. The depth average value $\langle a\rangle_z = 1.14\,\mathrm{m}^{-1}$ ($\langle a\rangle_z h_b = 23$) for the harvested profile, and $\langle a\rangle_z = 2.20\,\mathrm{m}^{-1}$ ($\langle a\rangle_z h_b = 44$) for the ripe profile.

The effective frond area density over the farm is defined as

$$\langle a\rangle_{xyz} = \frac{1}{L_{MF}L_y h_b}\int_0^{L_{MF}}\int_{-L_y/2}^{L_y/2}\int_{-h_b}^{0} a\,\mathrm{d}x\,\mathrm{d}y\,\mathrm{d}z. \tag{2.6}$$

The frond area density a takes the form depicted in figure 2 within the kelp rows and is 0 in the gaps between rows. The effective frond density thus decreases as the spacing between kelp rows increases, while keeping the row width unchanged.

Another set of farm arrangements (cases ‘B’) assumes a scenario where the kelp rows are positioned close enough so that there is no gap in between, i.e. essentially forming a uniform kelp farm block (figure 1*a*,*b*). The two profiles in figure 2 are employed in simulations involving this farm block configuration. Additionally, we conduct farm block simulations with varying effective density by introducing a multiplication factor to each frond density profile.

In the third set of farm arrangements (cases ‘PS’), the longlines are rotated by 90°, so that kelp rows are oriented parallel to the y-direction, perpendicular to the geostrophic flow (figure 1*e*,*f*). This set of arrangements also includes a range of values of S_{MF} and W_{MF}, mirroring the above-mentioned simulations with longlines aligned parallel to the x-direction.

Specifically, we have selected three simulations as representatives for an in-depth examination of the turbulence generation mechanisms. These selected cases are S26H (spaced farm rows parallel to the x-direction with a harvested profile, $S_{MF} = 26\,\mathrm{m}$ and $W_{MF} = 8\,\mathrm{m}$; refer to table 1) and B1H and B1R (i.e. farm block simulations with harvested and ripe profiles, respectively). By comparing these three simulations, we aim to elucidate the impacts of cross-stream spacing and the vertical frond area density profile on OML turbulence generation. The effects of effective density and kelp row orientation will be discussed subsequently, following the analysis of turbulence generation mechanisms.

3. Farm hydrodynamics

In this section we present the adjustment of mean flow to the kelp farm as well as the turbulence generated by the farm. We first introduce a flow decomposition to isolate distinct flow components. The instantaneous flow field can be split into the time-averaged and fluctuating components, i.e.

$$\boldsymbol{u}(x, y, z, t) = \bar{\boldsymbol{u}}(x, y, z) + \boldsymbol{u}'(x, y, z, t). \tag{3.1}$$

The overline represents the time average, and the prime represents temporal fluctuations about the time average. Further, the time-averaged flow field is decomposed into a cross-stream average and a steady cross-stream deviation

$$\bar{\boldsymbol{u}}(x, y, z) = \langle \bar{\boldsymbol{u}} \rangle_y (x, z) + \bar{\boldsymbol{u}}^c(x, y, z), \tag{3.2}$$

where $\langle \cdot \rangle_y$ denotes the spatial averaging in the y-direction.

The temporal and cross-stream average $\langle \bar{\boldsymbol{u}} \rangle_y$ is defined as the mean flow. The steady cross-stream deviation $\bar{\boldsymbol{u}}^c$ is referred to as the secondary flow component, representing the stationary circulation structure generated by lateral variations in farm geometry. Note that $\bar{\boldsymbol{u}}^c$ only exists in farm configurations with laterally spaced farm rows and is negligible in the farm block or in kelp rows that are perpendicular to the geostrophic flow (details shown in following sections). The transient fluctuation $\boldsymbol{u}'$ represents the turbulence component.

Similarly, the covariance between velocity and any field ϕ can be decomposed as

$$\left\langle \overline{\boldsymbol{u}\phi} \right\rangle_y = \langle \bar{\boldsymbol{u}} \rangle_y \left\langle \bar{\phi} \right\rangle_y + \left\langle \bar{\boldsymbol{u}}^c \bar{\phi}^c \right\rangle_y + \left\langle \overline{\boldsymbol{u}'\phi'} \right\rangle_y . \tag{3.3}$$

The first term on the right-hand side stands for the contribution from the mean flow; the second term represents the effect of the secondary flow, akin to a dispersive flux (Finnigan 2000); the third term represents the turbulent flux.

Specifically, we focus on three simulations, S26H, B1H and B1R, as representatives to illustrate the influences of kelp row spacing in the cross-stream direction and the vertical profiles of frond area density. Section 3.1 presents the adjustment of the time-mean flow field in the presence of kelp farms. Section 3.2 provides an overview of the hydrodynamic characteristics of all the different farm configurations. Section 3.3 compares the Langmuir circulation patterns across the three representative cases. Subsequently, we quantify turbulence and steady secondary flows in the three cases in § 3.4, and calculate the vertical velocity skewness in § 3.5 to characterize the turbulence generated by the farm.

3.1. *Mean flow*

The mean flow structure is substantially altered by the presence of kelp farms. Figure 3 shows the adjustment of mean flow in case S26H (spaced rows aligned with the x-direction) as an example. As flow enters the canopy region, the streamwise velocity decreases due to the drag force exerted by the kelp (figure 3*a*). A shear layer develops beneath the farm as a result of discontinuity in kelp frond density. In addition, vertical shear is also increased within the canopy due to the vertical variability of frond area density (figure 2). The shear within the farm is most pronounced near the leading edge, and gradually diminishes downstream as turbulence generated in the farm leads to vertical mixing of momentum.

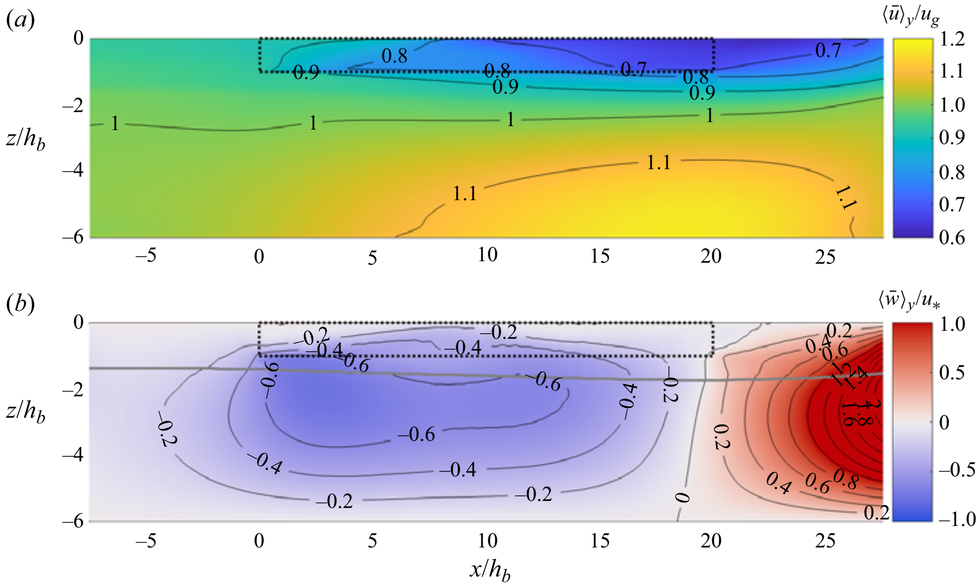

Figure 3. Side views of mean flow in case S26H (spaced rows aligned with the current, harvested profile). (*a*) Normalized streamwise velocity $\langle \bar{u} \rangle_y / u_g$. (*b*) Normalized vertical velocity $\langle \bar{w} \rangle_y / u_*$. The mean flow is averaged in time and in the cross-stream direction. Dotted rectangles show the extent of the farm, and the solid grey line in (*b*) represents the mixed layer depth. Note that $\langle \bar{u} \rangle_y$ is normalized by u_g and $\langle \bar{w} \rangle_y$ is normalized by u_*, and $\langle \bar{u} \rangle_y$ is generally much larger than $\langle \bar{w} \rangle_y$.

At the canopy leading edge, as the streamwise flow is decelerated by the pressure gradient set up by the canopy drag, the mean downward vertical velocity develops as a result of mass conservation (figure 3*b*). Likewise, the pressure decrease at the trailing edge induces an upward velocity in the farm's wake region. Note that a fringe region is located between the wake region and the downstream end of the domain (not shown), where the flow field is forced toward the precursor inflow conditions to avoid the wake effect on periodic horizontal boundary conditions. The farm-induced mean flow adjustment in case S26H closely aligns with the previous study by Yan *et al.* (2021); other cases involving different farm configurations will be explored further.

We define the mixed layer depth (MLD) z_i as the depth at which the laterally averaged potential temperature $\langle \bar{\theta} \rangle_y$ first deviates from its surface value by $\Delta\theta$ (e.g. Kara, Rochford & Hurlburt 2000), here using $\Delta\theta = 0.01$ K. The MLD is around 25 m at the upstream boundary where the inflow originates. The mixed layer deepens to nearly 40 m due to the downwelling created by the farm, which then recovers downstream from the farm. The farm is always situated above the pycnocline, and the buoyancy effect is thus considered to have negligible influence on turbulence generation within the farm.

The canopy drag length L_c is defined as (Belcher *et al.* 2003; Rominger & Nepf 2011; Belcher, Harman & Finnigan 2012)

$$L_c = \frac{2}{C_D \langle a \rangle_{xyz}}, \tag{3.4}$$

where C_D is the drag coefficient, and $\langle a \rangle_{xyz}$ is the effective frond density in (2.6). The factor of 2 in (3.4) accounts for the projection of frond surface area, as denoted by the term $\boldsymbol{P}$ in (2.5). The canopy drag length is $L_c = 347$ m for case S26H. Note that L_c varies with the effective density and thus the farm configuration, and case B1R (farm block,

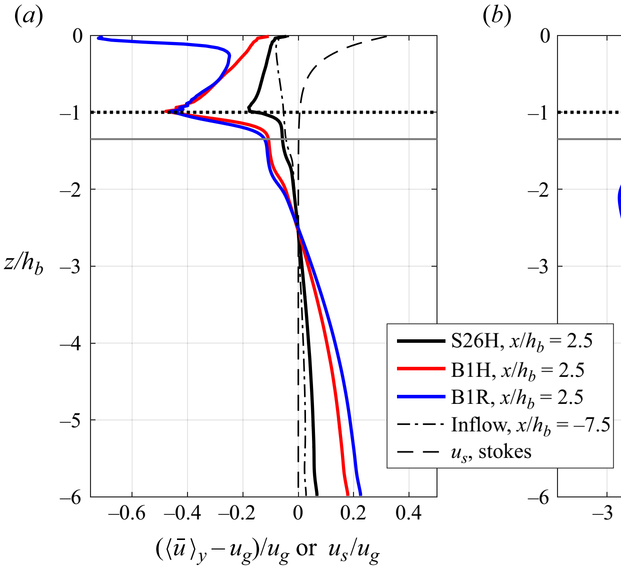

Figure 4. Vertical profiles of streamwise velocity $\langle \bar{u} \rangle_y$ (*a*) and vertical velocity $\langle \bar{w} \rangle_y$ (*b*). The velocities are time averaged and cross-stream averaged, at $x/h_b = 2.5$. Note that the geostrophic current $u_g = 0.2\,\mathrm{m\,s^{-1}}$ has been subtracted in (*a*). The streamwise velocity in (*a*) is normalized by u_g, and the vertical velocity in (*b*) is normalized by the friction velocity $u_* = 0.0061\,\mathrm{m\,s^{-1}}$. Black lines represent case S26H, spaced rows aligned with the geostrophic current, with the harvested profile; red lines represent case B1H, farm block with the harvested profile; blue lines represent case B1R, farm block with the ripe profile. Additionally, the dash-dotted line in (*a*) shows the streamwise velocity profile at the upstream boundary (inflow condition at $x/h_b = -7.5$). The dashed line in (*a*) represents the vertical profile of Stokes drift u_s. The dotted horizontal lines mark the farm bottom, and the thin solid horizontal lines represent the inflow MLD.

ripe profile) has the smallest L_c of 61 m. The length of the adjustment region scales in proportion to L_c, typically by a factor of 4.5–6 (Belcher *et al.* 2012). Therefore, the adjustment region length for the farm configurations in this study is either comparable to or larger than the farm length, suggesting that the canopy flow does not reach a fully developed state prior to exiting the farm. This explains the streamwise variations found in the mean flow field within the farm (figure 3) and also agrees with the analysis of the turbulence field presented in the following sections.

The mean flow properties in the other simulations B1H and B1R are compared with S26H (figure 4). The vertical profiles in figure 4 are averaged in the cross-stream direction, and also averaged in the streamwise direction from the leading edge to $5h_b$ into the farm, a distance comparable to the canopy drag length L_c in cases B1H and B1R. Generally cases B1H and B1R are similar to case S26H shown above, except that B1H and B1R demonstrate more pronounced downwelling at the leading edge and stronger vertical shear below the canopy, due to their higher effective frond area density and greater drag. In addition, the vertical shear of the mean streamwise flow within the farm is also stronger in B1H compared with S26H, because of the higher effective density in B1H. Moreover, while the streamwise mean velocity monotonically increases from the canopy bottom to the sea surface in cases S26H and B1H, the vertical shear reverses near the surface in B1R, because the presence of the uppermost dense layer in B1R locally enhances drag and decelerates flow.

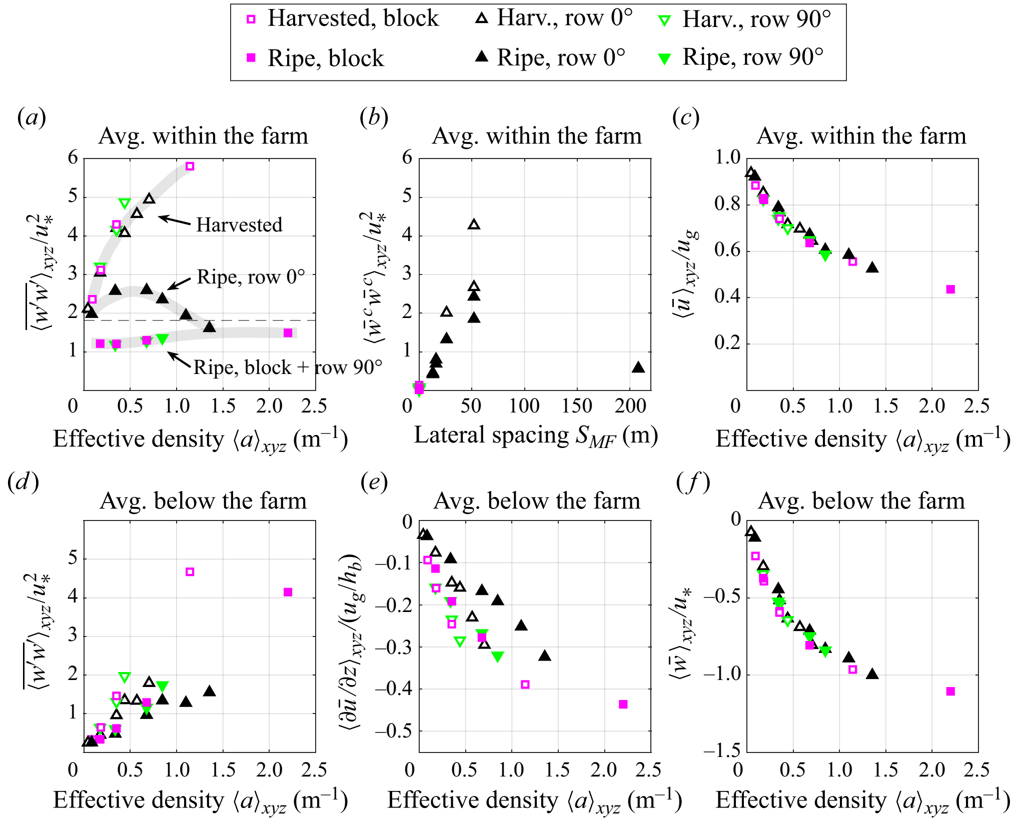

Figure 5. Mean flow ($\bar{u}$, $\bar{w}$, and shear $\partial\bar{u}/\partial z$), secondary flow ($\bar{w}^c$) and turbulence ($w'$) statistics within the farm (*a–c*) and below the farm (*d–f*). Each point represents a simulation (see the legends for details). Note that row 0° and row 90° denote kelp rows aligned with and perpendicular to the current, respectively. The horizontal dashed line in (*a*) represents the intensity of standard Langmuir turbulence in the absence of a farm. The thick grey lines in (*a*) are fitting curves for the three types of farm configurations. Averaging within the farm is conducted between $z = 0$ and $-h_b$, and averaging below the farm is between $-h_b$ and $-2h_b$. The horizontal axis in (*a,c–f*) is the effective density $\langle a \rangle_{xyz}$ averaged within the farm. Note that the shear and vertical velocity are negative below the farm in (*e,f*). The mean streamwise velocity is normalized by the geostrophic velocity $u_g = 0.2\,\mathrm{m\,s^{-1}}$, the mean vertical velocity is normalized by the friction velocity $u_* = 0.0061\,\mathrm{m\,s^{-1}}$ and the variance terms are normalized by u_*^2.

Note that the selected cases have a relatively high effective density $\langle a \rangle_{xyz}$. Other simulations that are not presented here, e.g. with larger spacing between kelp rows or with a lower frond area density, generally have weaker downwelling at the farm leading edge and weaker shear in the mean streamwise flow.

3.2. *Overview*

Along with modifications to the mean flow, the presence of the farm also affects Langmuir circulation patterns and turbulence intensity. In this section, we present an overview of the distinct flow patterns associated with various farm configurations, before moving on to detailed analysis of Langmuir circulation and turbulence. The magnitudes of mean flow, secondary flow and turbulence components within and below the canopy are summarized in figure 5 for all the farm configurations in table 1.

The mean streamwise flow within the farm decreases with the increased effective density $\langle a\rangle_{xyz}$ due to the greater kelp drag (figure 5*c*), leading to stronger downwelling below the farm as a result of mass conservation (figure 5*f*). In the shear layer below the canopy, the vertical shear of streamwise mean flow generally increases in magnitude with the increased effective frond density (figure 5*e*). Correspondingly, the turbulence intensity in the shear layer – quantified by the variance of the temporal fluctuating component of vertical velocity $\langle\overline{w'w'}\rangle_{xyz}$ – increases with the increased $\langle a\rangle_{xyz}$ (figure 5*d*). This is consistent with that expected for classical canopy flow, where the canopy effect positively depends on $\langle a\rangle_{xyz}$ (e.g. Poggi *et al.* 2004; Bailey & Stoll 2013). For shear layer statistics, the average is calculated within a vertical distance equal to h_b beneath the canopy bottom, i.e.

$$\langle\cdot\rangle_{xyz} = \frac{1}{L_{MF}L_y h_b}\int_0^{L_{MF}}\int_{-L_y/2}^{L_y/2}\int_{-2h_b}^{-h_b}\cdot\,\mathrm{d}x\,\mathrm{d}y\,\mathrm{d}z, \tag{3.5}$$

for averaging below the farm. Here, we select the vertical component w' because of its direct relevance to vertical transport in kelp farms. More discussions about the other components u' and v' and turbulence anisotropy will be presented later. Note that the scatter in figure 5(*d*,*e*) primarily results from the two different vertical profiles of frond area density. The dense layer near the surface in the ripe profile has a small influence on the shear layer dynamics below the canopy, and excluding this dense surface layer from the effective density calculation can lead to improved alignment in figure 5(*d*,*e*).

As a contrast to the shear layer turbulence generated below the canopy, turbulence intensity within the farm displays a more complex dependence on the effective frond density (figure 5*a*). Note that, within this depth range, e.g. between the sea surface and $z=-h_b$, standard Langmuir turbulence is expected to occur in the absence of the canopy (McWilliams *et al.* 1997). In the presence of the canopy, for kelp frond density with the harvested vertical profile, $\langle\overline{w'w'}\rangle_y$ is enhanced compared with that of the standard Langmuir turbulence. Moreover, the intensity of enhanced turbulence within the farm positively depends on the effective density $\langle a\rangle_{xyz}$. However, for farm configurations with the ripe vertical profile, turbulence is inhibited in farm blocks and kelp rows that are perpendicular to the geostrophic current. For farms with kelp rows aligned with the current, $\langle\overline{w'w'}\rangle_y$ is enhanced compared with the standard Langmuir turbulence only for cases with an intermediate effective density $\langle a\rangle_{xyz}$. This enhancement diminishes as $\langle a\rangle_{xyz}$ increases, i.e. with closely spaced rows that asymptotically resemble a farm block, or, as $\langle a\rangle_{xyz}$ decreases, asymptoting toward a scenario without a farm.

For canopy flow without the influence of waves and Langmuir circulation, the turbulence intensity within the canopy is usually anticipated to decrease with increased effective density, due to the weaker penetration of shear layer eddies (Poggi *et al.* 2004; Bailey & Stoll 2013). Nevertheless, our simulations show that the turbulence intensity in the farm either positively depends on the effective density or exhibits a more complex dependence. This contrasting dependence on effective density underscores the distinct type of turbulence that arises from the interaction between the canopy and the OML, which is called the farm-generated Langmuir turbulence and will be presented in the following sections.

Moreover, secondary flow $\langle\bar{w}^c\bar{w}^c\rangle_y$ (stationary circulation) can be generated within the farm exclusively in cases with kelp rows aligned with the current (figure 5*b*). The occurrence of stationary secondary circulation associated with spaced kelp rows is consistent with the previous study by Yan *et al.* (2021), who referred to these flow patterns as 'attached Langmuir circulation'. The intensity of $\langle\bar{w}^c\bar{w}^c\rangle_y$ is always stronger in cases with the harvested profile compared with the ripe profile. Our simulations do not allow for a clear identification of the maximum intensity with respect to the lateral spacing S_{MF}, and the peak of $\langle \bar{w}^c \bar{w}^c \rangle_y$ appears to fall within the range of $S_{MF} = 52$ m and 208 m. Note that secondary flow never occurs in the shear layer below the canopy.

Overall, these various flow statistics highlight the distinction between the hydrodynamics within the farm (within the OML where Langmuir turbulence is expected) and the classical shear layer turbulence beneath the farm. In addition, the contrast between different farm simulations suggests that these hydrodynamic processes depend on both the vertical frond density profile and horizontal farm arrangement, and these factors will be analysed in detail below.

3.3. *Langmuir circulations*

Three representative simulations are selected to investigate the distinct flow patterns associated with different farm configurations, i.e. case S26H (spaced rows aligned with the x-direction, harvested profile), case B1H (farm block, harvested profile) and case B1R (farm block, ripe profile). Snapshots of instantaneous vertical velocities of the three simulations are compared in figure 6, on a horizontal plane at $z = -0.25h_b$.

Upstream of the farm, the elongated streaks of downward vertical velocity are indicative of standard Langmuir circulation (e.g. McWilliams *et al.* 1997). These patterns are typically featured by stronger downward motions within narrower regions compared with the broader and weaker upward motions. In addition, the streaks are generally rotated to the right of the direction of the wind and waves (x-direction) as a result of Coriolis. The standard Langmuir circulation patterns are transient, characterized by their continuous cycles of formation, evolution and dissipation.

For the case with laterally spaced kelp rows (case S26H), Langmuir circulation within the farm area shows a notable increase in magnitude compared with the standard Langmuir circulation in the upstream region (figure 6*a*). Moreover, these Langmuir circulation patterns are locked in space in the cross-stream direction, generally with upward motions within the kelp rows and downward motions within the gaps in between. The Langmuir patterns in the farm are generally stationary in time, although the smaller-scale coherent structures are still transient. These patterns are termed as the 'attached Langmuir circulation' (Yan *et al.* 2021) because of their locked-in-space characteristics.

For the farm block case with the harvested profile (case B1H), Langmuir circulation is also enhanced within the farm compared with the upstream region (figure 6*b*). However, these farm-enhanced Langmuir circulation patterns are completely transient and not locked in space due to the absence of repeated kelp rows, and we thus refer to these patterns as 'unattached Langmuir circulation'. In the vertical direction, both the attached and unattached Langmuir circulation patterns have comparable dimensions to the farm height, with their maximum intensity found at a depth of around 10 m (quantitative results shown in § 3.4).

Furthermore, in contrast to the Langmuir patterns found in case B1H, Langmuir circulation notably vanishes in the farm in case B1R (farm block with the ripe profile, see figure 6*c*). This implies an absence of the Langmuir circulation generation mechanism or an increase in dissipation in case B1R, as will be investigated below. It is also worthwhile noting that the vertical velocity exhibits patterns aligned with the lateral direction in case B1R, in contrast to the streaks aligned with the streamwise direction in other cases. These distinct patterns in case B1R (e.g. for x/h_b from 5 to 10) correspond to shear-generated turbulence within the farm, as the canopy drag force significantly decelerates flow near the

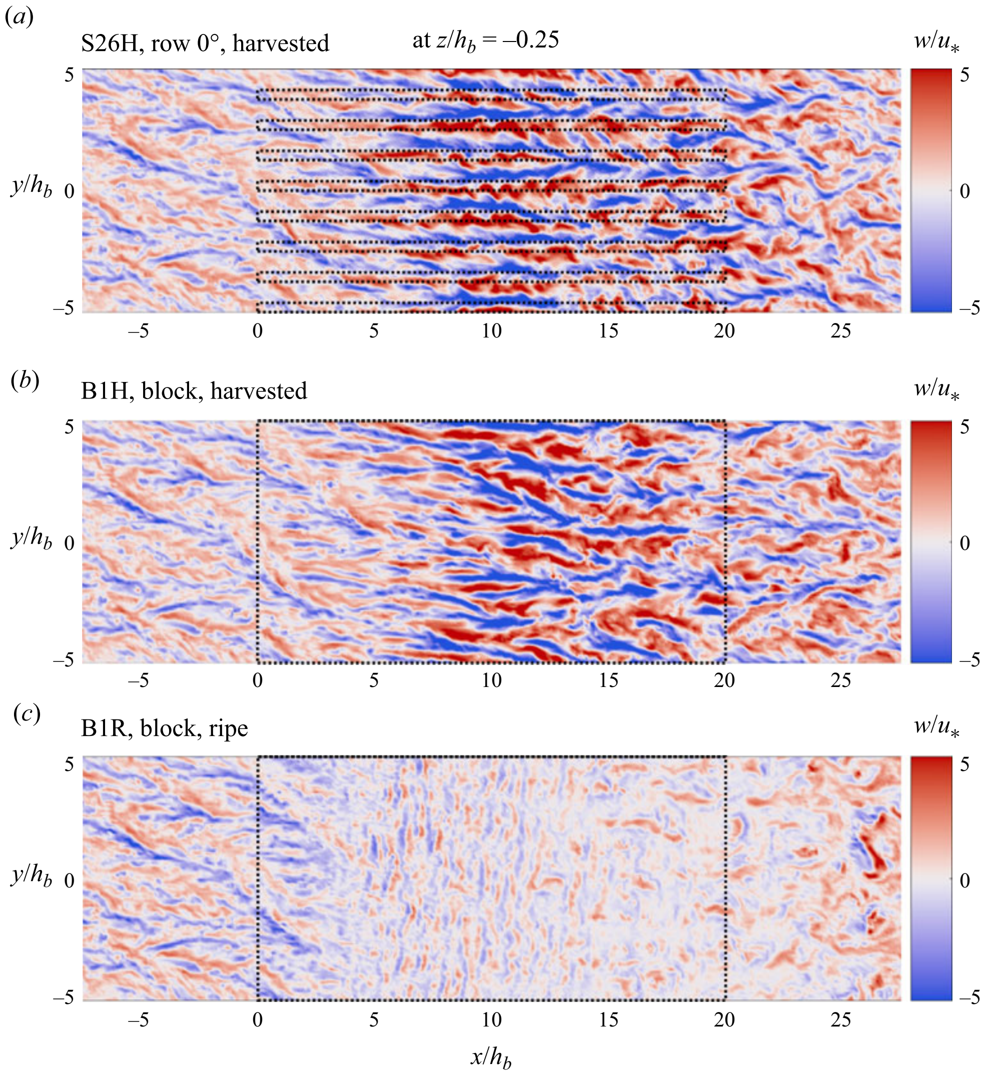

Figure 6. Snapshots of normalized vertical velocity w/u_* on a horizontal plane at $z = -0.25h_b$, for cases S26H (*a*), B1H (*b*) and B1R (*c*). Dotted rectangles show the extent of the farm block or rows.

sea surface and enhances the vertical shear (figure 4*a*). Moreover, shear layer turbulence generated at the farm bottom edge could penetrate into the farm in cases where Langmuir turbulence is inhibited (e.g. for $x/h_b > 15$ in figure 6*c*). The distinct Langmuir patterns as well as the penetration of shear layer eddies will be further analysed in subsequent sections.

Additionally, a simulation with laterally spaced kelp rows with the ripe profile (case S26R) is examined. In this case, attached Langmuir circulation is generated in the farm (not shown) that resembles the patterns found in case S26H, while the magnitude of vertical velocity is smaller in case S26R compared with S26H.

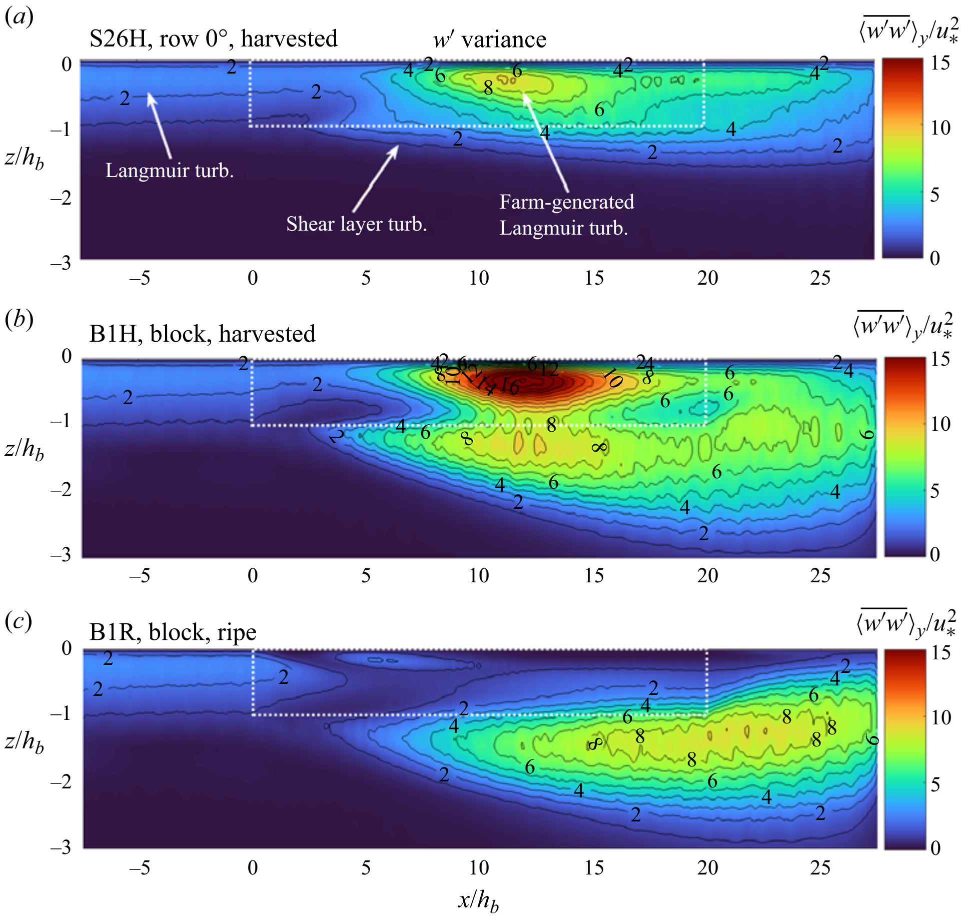

Figure 7. Side views of the transient component of vertical velocity variance $\langle \overline{w'w'} \rangle_y / u_*^2$ for cases S26H (*a*), B1H (*b*) and B1R (*c*). The results are temporally and laterally averaged. Dotted rectangles show the extent of the farm.

3.4. *Langmuir turbulence and bottom shear layer turbulence*

The temporally and laterally averaged vertical velocity variance associated with transient eddies ($\langle \overline{w'w'} \rangle_y$) is calculated to quantify the farm-generated turbulence (figure 7). The vertical component w' is selected because Langmuir turbulence is usually characterized by its large vertical velocity variance (McWilliams *et al.* 1997; Yan *et al.* 2021), and the vertical component also directly influences vertical transport.

Standard Langmuir turbulence occurs upstream of the farm, with the maximum $\langle \overline{w'w'} \rangle_y$ found slightly below the sea surface, e.g. around 5–10 m, consistent with McWilliams *et al.* (1997). Within the farm, similar Langmuir-type turbulence is generated in the two cases with the harvested profile (B1H and S26H, figure 7*a*,*b*). The farm-generated Langmuir turbulence has a stronger magnitude compared with the standard Langmuir turbulence in the upstream region, while its vertical variance $\langle \overline{w'w'} \rangle_y$ also peaks at a similar depth of around 5–10 m. In the streamwise direction, the intensity of farm-generated Langmuir turbulence increases from the leading edge of the farm as flow adjusts to the canopy drag, with a maximum at around $x/h_b = 10$ (also see figure 9). Turbulence intensity then decreases toward the farm trailing edge, due to the decrease in the production mechanisms and the damping by kelp drag and viscosity (details examined in the energy budget calculation in § 4). In addition, the farm-generated Langmuir turbulence is stronger in the farm block case B1H than the spaced rows case S26H (both with a harvested profile), and this aligns with the positive dependence on effective frond area density in figure 5(*a*). By contrast, no intensified turbulence is found in the farm block with a ripe profile (case B1R) (figure 7*c*), consistent with the absence of Langmuir patterns in the map view plot of vertical velocity (figure 6*c*).

The intensified turbulence in the kelp farm is referred to as Langmuir type because its generation relates to the Stokes drift (see § 4), akin to the standard Langmuir turbulence. Furthermore, the intensified Langmuir-type turbulence in the farm completely disappears in another set of test cases (S26H-NW, B1H-NW, B1R-NW, not presented here), where the surface wave forcing is excluded. This provides corroborating evidence that the Langmuir-type turbulence results from the interaction between waves and canopy flow.

In addition to the Langmuir-type turbulence generated within the farm, shear layer turbulence occurs at the bottom edge of the canopy. The shear layer turbulence, as a characteristic of classical canopy flow, is consistently found across all the simulations regardless of the presence or absence of Langmuir-type turbulence within the farm. The intensity of shear layer turbulence typically increases with the increased effective density (e.g. Bailey & Stoll 2013), so that the farm block cases (B1H and B1R) exhibit stronger turbulence below the farm compared with the case with spaced kelp rows (S26H).

While the shear layer turbulence mostly occurs beneath the canopy, it also penetrates into the canopy, in particular in the downstream part of the farm. Nevertheless, the penetrated shear layer turbulence is overall much weaker than the farm-generated Langmuir turbulence (as will be substantiated by the skewness analysis in § refsec:results-skewness). Therefore, in cases with enhanced Langmuir turbulence, shear layer turbulence has a minimal influence on the turbulence statistics calculated within the farm. This point is also supported by the dependence of turbulence intensity on the effective density $\langle a\rangle_{xyz}$ in figure 5(*a*). Turbulence intensity within the canopy is expected to decrease with increased $\langle a\rangle_{xyz}$, assuming penetration of shear layer is the dominant source of turbulence (Poggi *et al.* 2004; Bailey & Stoll 2013). Nevertheless, our simulations show a more complex dependence of turbulence intensity on $\langle a\rangle_{xyz}$, due to the dominance of Langmuir-type turbulence within the farm.

We have primarily focused on the vertical component w', and the horizontal components u' and v' generally display similar distributions to w'. However, it is worthwhile noting that the transient eddies are not isotropic, and this turbulence anisotropy also provides insights into distinguishing between different types of farm-generated turbulence. The shear layer turbulence typically has a stronger streamwise component u' compared with the other components, while the Langmuir-type turbulence features a relatively stronger vertical component w'.

In figure 8, we plot the temporally and laterally averaged vertical velocity variance associated with the steady secondary flow, denoted as $\langle \bar{w}^c\bar{w}^c\rangle_y$. Note that secondary flow includes both the lateral variations in streamwise velocity ($\bar{u}^c$) and the stationary lateral circulation ($\bar{v}^c$ and $\bar{w}^c$). Secondary flow exclusively occurs in the case with laterally spaced kelp rows (case S26H), where attached Langmuir circulation occurs. In farm block simulations where transient Langmuir circulation has been found, $\langle \bar{w}^c\bar{w}^c\rangle_y$ is generally negligible. The region of high $\langle \bar{w}^c\bar{w}^c\rangle_y$ roughly coincides with that of high $\langle \overline{w'w'}\rangle_y$ for case S26H, while the peak of $\langle \bar{w}^c\bar{w}^c\rangle_y$ is slightly upstream of $\langle \overline{w'w'}\rangle_y$ (figure 9).

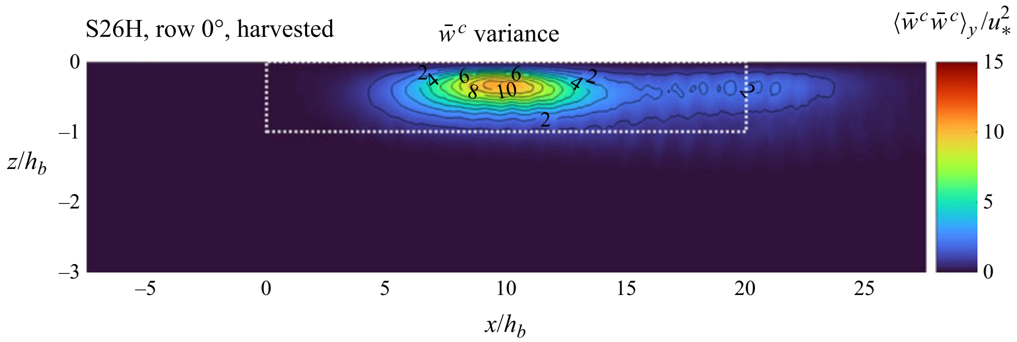

Figure 8. Side view of the secondary flow component of vertical velocity variance $\langle \bar{w}^c \bar{w}^c \rangle_y / u_*^2$ for cases S26H. The results are temporally and laterally averaged. The dotted rectangle shows the extent of the farm.

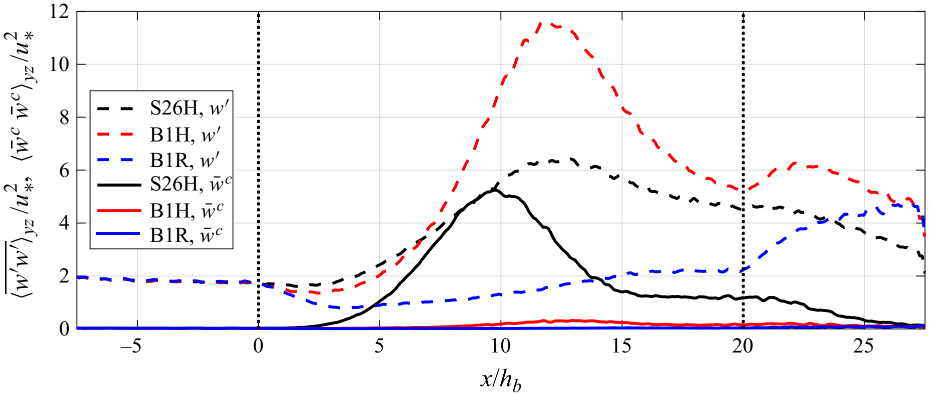

Figure 9. Streamwise variations of $\langle \overline{w'w'} \rangle_y / u_*^2$ (dashed lines) and $\langle \bar{w}^c \bar{w}^c \rangle_y / u_*^2$ (solid lines) for cases S26H (black), B1H (red) and B1R (blue). The results are temporally, laterally and vertically ($z = 0$ to $-h_b$) averaged. Vertical dotted lines show the extent of the farm.

We calculated the lateral-direction wavenumber spectra of the vertical velocity to investigate the characteristic lateral spacing of Langmuir circulations. In case S26H (rows with a spacing of 26 m), the spectral peak in the farm aligns with the lateral row spacing $S_{MF} = 26$ m (figure 10*a*). Similarly, for case S52H with rows spaced at 52 m, the peak wavelength corresponds to $S_{MF} = 52$ m. Note that these spectra are calculated from the total vertical velocity w, and the energy peaks in the above two cases are predominantly contributed by the secondary flow component $\bar{w}^c$. The peaks would be considerably less distinct if calculating the spectra using the turbulent component w' alone. In case B1H (farm block with the harvested profile), the spectral peak corresponds to a wavelength of around 30 m (figure 10*b*). This peak wavelength is slightly smaller than that of the inflow condition with standard Langmuir turbulence. In contrast to the spaced rows, the farm block exhibits a less distinct peak, due to the absence of secondary flow structures caused by row spacing. For case B1R (farm block with the ripe profile), the spectrum exhibits no apparent peak because of the inhibition of Langmuir turbulence in the farm, with a weakened overall magnitude compared with that upstream of the farm.

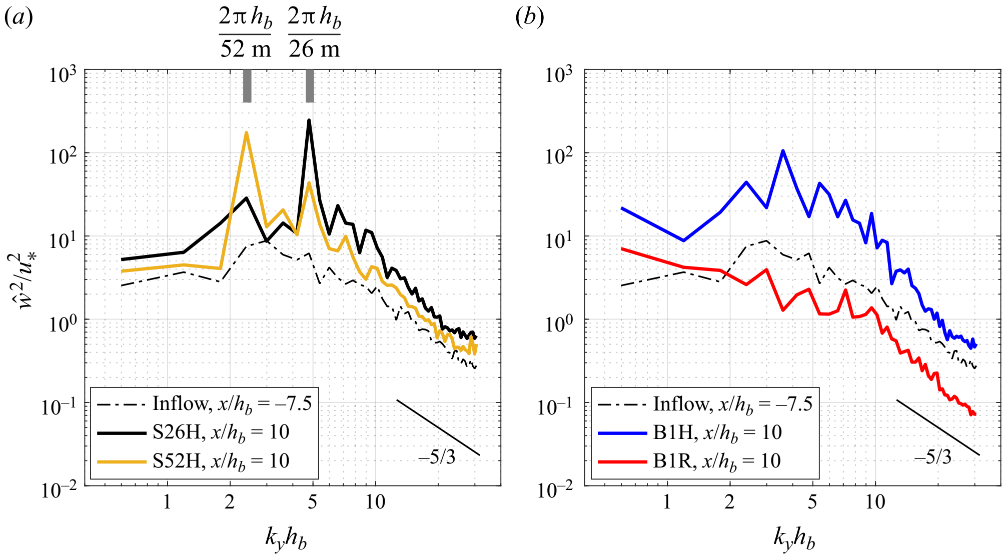

Figure 10. Spectra of the vertical velocity vs the lateral-direction wavenumber k_y. (*a*) Cases S26H (rows aligned with the x-direction, 26 m spacing, solid black line) and S52H (52 m spacing, solid yellow line), at $x/h_b = 10$ and averaged between $z = 0$ and $z = -h_b$. The dash-dotted black line represents the inflow condition at the upstream boundary ($x/h_b = -7.5$). Two vertical grey lines indicate the corresponding spacing between kelp rows, 26 and 52 m, respectively. (*b*) Cases B1H (solid blue line) and B1R (solid red line).

3.5. *Vertical velocity skewness*

The skewness of the vertical turbulence component, defined as $\langle\overline{w'^3}\rangle_y/\langle\overline{w'^2}\rangle_y^{3/2}$, is plotted in figure 11 to illustrate the distinct attributes of various types of turbulence. The standard Langmuir turbulence in the upstream region is characterized by its negative skewness of vertical velocity (McWilliams *et al.* 1997). The negative skewness indicates stronger downward motions confined within narrower regions in comparison with broader and weaker upward motions, consistent with the Langmuir circulation patterns shown in figure 6.

In the shear layer generated at the canopy bottom, the vertical velocity skewness is generally negative beneath the canopy and positive near the canopy edge (figure 11). The positive skewness of vertical velocity near the canopy edge indicates the dominance of sweep events that bring high-momentum fluid into the canopy, consistent with those found in classical canopy flow without waves (Raupach & Thom 1981; Katul *et al.* 1997; Poggi *et al.* 2004). Note that the skewness sign in the suspended canopy is opposite to that of submerged benthic canopies due to the reversed geometry of the problem set-ups (i.e. here sweep events are characterized by intensified positive vertical velocities into the canopy). Conversely, the negative skewness of vertical velocity below the canopy is indicative of the prevalence of ejection events.

The vertical velocity skewness of the farm-generated Langmuir turbulence appears less clear, displaying mostly negative values. However, the boundary between shear layer turbulence and farm-generated Langmuir turbulence remains discernible through their difference in the skewness sign inside the canopy. Specifically, in case B1H in figure 11(*b*), the positive vertical velocity skewness associated with shear layer turbulence occupies less than one third of the canopy height. Furthermore, the region with the highest turbulence intensity is located above the region with positive skewness (figure 7*b*), underscoring that

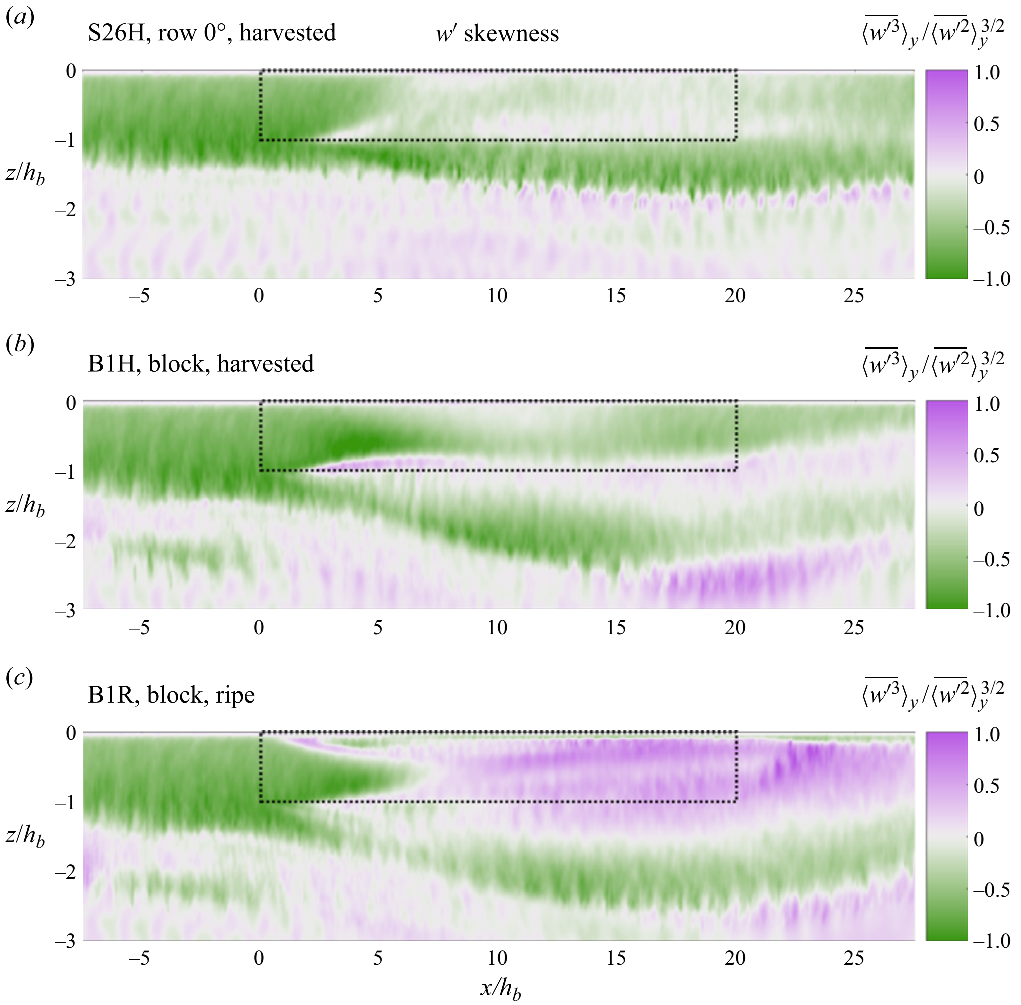

Figure 11. Side views of the skewness of w' (transient component of vertical velocity) for cases S26H (*a*), B1H (*b*) and B1R (*c*). The results are temporally and laterally averaged. Dotted rectangles show the extent of the farm.

the majority of energy within the farm is attributed to Langmuir-type turbulence rather than the penetrated shear layer turbulence.

For case B1R (farm block with the ripe profile), the concept of skewness within the farm lacks significance due to the absence of Langmuir-type turbulence. However, indications of shear-generated turbulence can be found within the farm, e.g. in the range of x/h_b from 0 to 5, where the mean flow is adjusting to the canopy drag (figure 11*c*). This shear-generated turbulence within the farm exhibits similar characteristics to the shear layer turbulence below the canopy bottom edge, although with lower intensity. It results from the vertical variability in frond area density, and then rapidly dissipates downstream in the farm.

Similarly, we define a skewness for the steady secondary flow as $\langle\bar{w}^{c3}\rangle_y/\langle\bar{w}^{c2}\rangle_y^{3/2}$. The steady secondary velocity is generally upward in the kelp rows and downward in the gaps between kelp rows (figure 6). In cases where the kelp rows are narrower than the gaps, e.g. case S26H in figure 12, the upward secondary flow is typically stronger in magnitude than

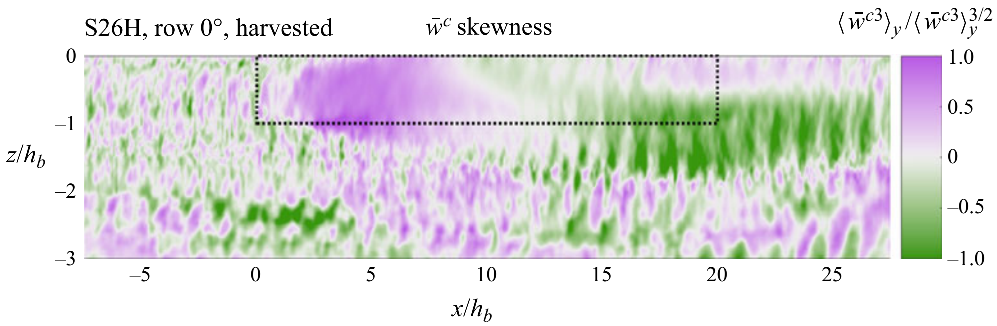

Figure 12. Side view of the skewness of $\bar{w}^c$ (steady secondary flow component of vertical velocity) for case S26H. The results are temporally and laterally averaged. The dotted rectangle shows the extent of the farm.

the downward flow as a result of mass balance. Therefore, a positive skewness of the steady secondary vertical velocity is evident in the upstream part of the farm (figure 12). Toward the downstream region of the farm, the vertical secondary velocity skewness becomes less distinct. This can be attributed to the lateral expansion of Langmuir wakes linked to kelp rows, so that regions of upwelling may extend beyond the constraints of kelp rows (figure 6*a*, also see Appendix B for a clearer presentation of the Langmuir wake pattern in case S208H, the single-row simulation). As one may anticipate, the skewness of secondary flow varies with changes in farm width and lateral spacing across different farm configurations. As an example, the skewness $\langle \bar{w}^{c3}\rangle_y/\langle \bar{w}^{c2}\rangle_y^{3/2}$ in case S208H can reach up to a value of 3, where the upwelling of secondary flow is confined within a single kelp row before wake expansion occurs.

The skewness of turbulence and secondary flow investigated above also influences diffusive and dispersive fluxes in the farm, potentially leading to asymmetric vertical nutrient transport (Wyngaard & Brost 1984; Wyngaard & Weil 1991; Chor, McWilliams & Chamecki 2020, 2021). Note that spurious oscillations displaying alternating positive and negative skewness can be found in the secondary flow and turbulence components, e.g. around $z/h_b = -2$ and $x/h_b = 15$ in figure 12 and around $z/h_b = -2$ and $x/h_b = 20$ in figure 11(*a*). These oscillations occur in regions where $\bar{w}^c$ or w' is minimal and thus do not have practical significance.

4. Kinetic energy balance

In this section we investigate the kinetic energy equations to understand the sources of Langmuir circulation and turbulence. Following the convention in (3.2) and (3.3), we decompose the total kinetic energy K_T into the mean flow energy K_M, secondary flow energy K_{SE} and turbulence kinetic energy K_{TE}, i.e.

$$K_T = \frac{1}{2}\langle \overline{u_i u_i}\rangle_y = \underbrace{\frac{1}{2}\langle \overline{u_i}\rangle_y \langle \overline{u_i}\rangle_y}_{K_M} + \underbrace{\frac{1}{2}\left\langle \overline{u_i}^c \overline{u_i}^c\right\rangle_y}_{K_{SE}} + \underbrace{\frac{1}{2}\left\langle \overline{u_i' u_i'}\right\rangle_y}_{K_{TE}}. \tag{4.1}$$

We can derive the transport equations for K_M, K_{SE} and K_{TE} from the governing equations (2.1) and (2.2) (Yan *et al.* 2021)

$$\frac{\mathrm{D}K_M}{\mathrm{D}t} = -C_{M-SE} - C_{M-TE} + S_M + D_M + T_M + R_M, \tag{4.2a}$$

$$\frac{\mathrm{D}K_{SE}}{\mathrm{D}t} = C_{M-SE} - C_{SE-TE} + S_{SE} + D_{SE} + T_{SE}, \tag{4.2b}$$

$$\frac{\mathrm{D}K_{TE}}{\mathrm{D}t} = C_{M-TE} + C_{SE-TE} + S_{TE} + \epsilon_{TE} + D_{TE} + T_{TE}. \tag{4.2c}$$

Here, the material derivative is $\mathrm{D}/\mathrm{D}t = \partial/\partial t + \langle \overline{u_j} \rangle_y \partial/\partial x_j + u_s \partial/\partial x$. Note that we have neglected the buoyancy production terms, as the farm is located within the OML. Terms C_{M-SE}, C_{M-TE} and C_{SE-TE} represent the energy conversion between the mean flow K_M, secondary flow K_{SE} and turbulence K_{TE} (also referred to as shear production), written as

$$C_{M-SE} = -\left\langle \overline{u_i}^c \overline{u_j}^c \right\rangle_y \frac{\partial \langle \overline{u_i} \rangle_y}{\partial x_j}, \tag{4.3a}$$

$$C_{M-TE} = -\left\langle \overline{u_i' u_j'} \right\rangle_y \frac{\partial \langle \overline{u_i} \rangle_y}{\partial x_j}, \tag{4.3b}$$

$$C_{SE-TE} = -\left\langle \overline{u_i' u_j'} \frac{\partial \overline{u_i}^c}{\partial x_j} \right\rangle_y. \tag{4.3c}$$

Terms S_M, S_{SE} and S_{TE} stand for Stokes production that transfers energy between waves and the three flow components, and are given by

$$S_M = -\langle \bar{u} \rangle_y \langle \bar{w} \rangle_y \frac{\partial u_s}{\partial z}, \quad S_{SE} = -\left\langle \bar{u}^c \bar{w}^c \right\rangle_y \frac{\partial u_s}{\partial z}, \quad S_{TE} = -\left\langle \overline{u' w'} \right\rangle_y \frac{\partial u_s}{\partial z}. \tag{4.4a–c}$$

The SGS dissipation term is

$$\epsilon_{TE} = -\left\langle \overline{\tau_{ij}' \frac{\partial u_i'}{\partial x_j}} \right\rangle_y. \tag{4.5}$$

The majority of energy dissipation is expected to occur in the small-scale transient eddies for turbulent flows with a large Reynolds number (e.g. Pope 2000). Therefore, the energy loss of the larger-scale mean flow and secondary flow due to direct SGS dissipation is considered negligible, and we only focus on the dissipation of turbulence kinetic energy. The canopy drag dissipation terms are

$$D_M = -\langle \overline{u_i} \rangle_y \left\langle \overline{F_{D,i}} \right\rangle_y, \quad D_{SE} = -\left\langle \overline{u_i}^c \overline{F_{D,i}}^c \right\rangle_y, \quad D_{TE} = -\left\langle \overline{u_i' F_{D,i}'} \right\rangle_y, \tag{4.6a–c}$$

which represent the energy loss or gain associated with canopy drag. In addition, several flux terms representing kinetic energy transport associated with the resolved stress, SGS stress and pressure are collected into the transport terms T_M, T_{SE} and T_{TE}. The last term $R_M = f \langle \bar{v} \rangle_y (u_g - u_s)$ in the mean flow energy budget represents the energy transfer between the mean flow, surface waves and the background geostrophic current, resembling the concept of Stokes–Coriolis work (Suzuki & Fox-Kemper 2016; Yan *et al.* 2021).

We calculate the turbulent kinetic energy budget for case B1H (farm block with the harvested profile), and the major source and sink terms are shown in figure 13. The Stokes production is the dominant source of turbulence upstream of the farm, where standard Langmuir turbulence is found. This agrees with the widely recognized mechanism wherein the generation of Langmuir circulation results from vorticity tilting by the Stokes drift (Craik 1977; Leibovich 1977, 1983). Within the farm, the Stokes production becomes significantly stronger, which, together with the shear production, contributes to the enhanced Langmuir-type turbulence (figures 13 and 7). Below the farm, shear production

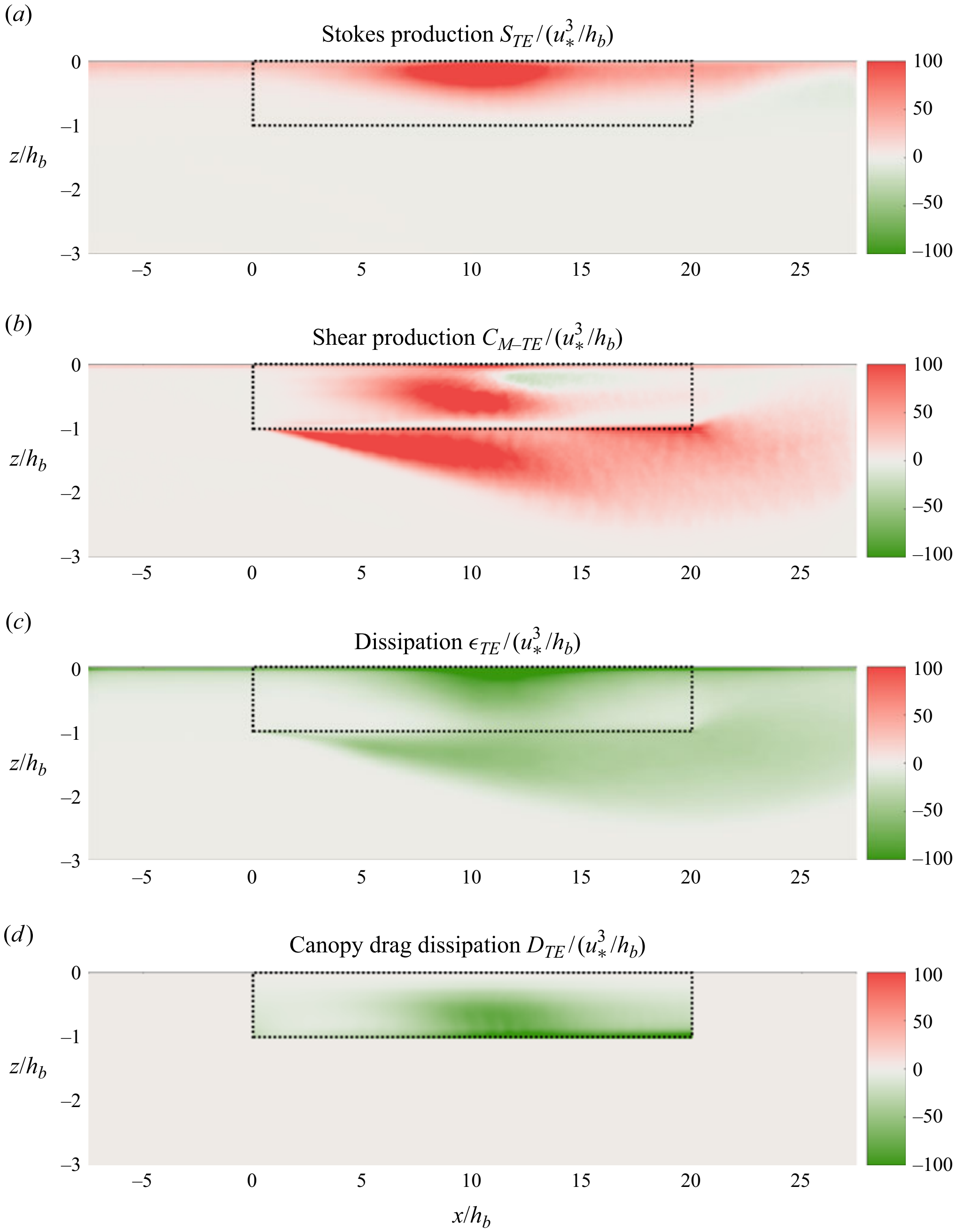

Figure 13. Side views of terms in the K_{TE} budget in (4.2*c*) for case B1H (farm block, harvested profile). The results are temporally and laterally averaged. Dotted rectangles show the extent of the farm.

provides the dominant source of shear layer turbulence, and Stokes production is weak because the Stokes drift diminishes at greater depth. Both dissipation and canopy drag dissipation terms tend to destroy the turbulence generated within the farm, while in the shear layer below the canopy, the dissipation term is the only sink of turbulence

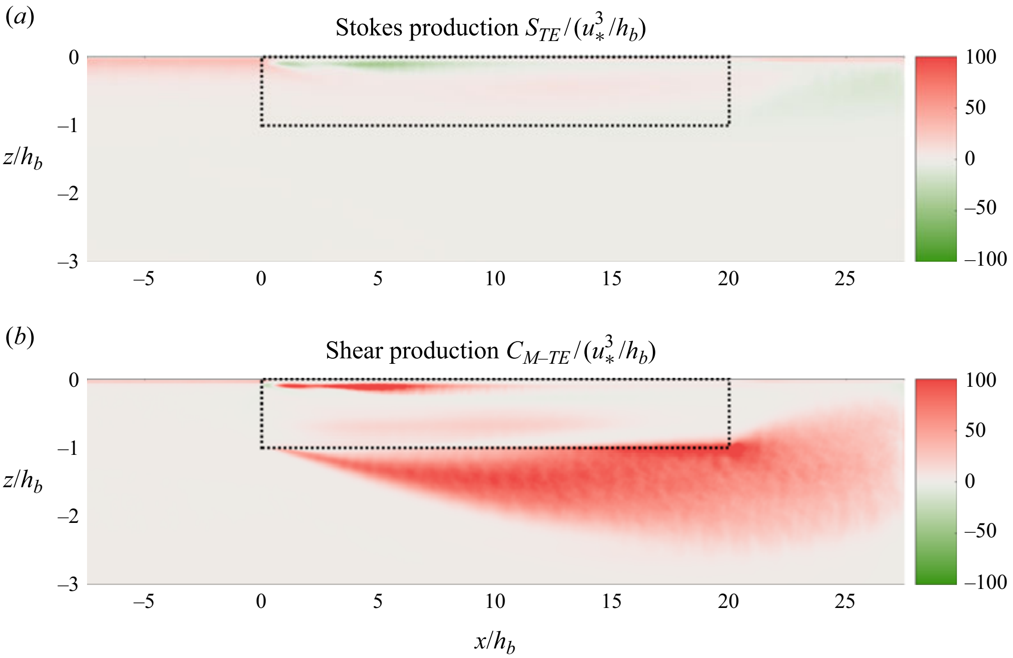

Figure 14. Side views of terms in the K_{TE} budget in (4.2c) for case B1R (farm block, ripe profile). The results are temporally and laterally averaged. Dotted rectangles show the extent of the farm. Note that differences between case B1R and case B1H (figure 13) primarily lie in the energy production mechanisms. The dissipation and canopy drag dissipation terms are not shown here because the energy loss mechanisms in case B1R are similar to case B1H.

kinetic energy. Note that the secondary flow energy is negligible in the farm block, and there is no energy conversion associated with secondary flow.

In case B1R (farm block with the ripe profile), the shear production term is the major source of turbulence kinetic energy in the shear layer below the canopy (figure 14), consistent with case B1H discussed above (farm block with the harvested profile). However, when focusing within the farm, both the Stokes production and shear production diminish due to the presence of a dense layer near the surface (characteristic of the ripe profile). This explains the absence of Langmuir-type turbulence in figure 7(c). In particular, negative values of Stokes production are even found near the sea surface, indicating that the shear of the Stokes drift velocity contributes to disrupting vortex formation rather than stretching vortex tubes (detailed mechanisms are explained in § 5). Negative vertical shear of the Eulerian velocity arises due to the presence of a dense kelp layer near the surface, which dominates over the positive vertical shear of the Stokes drift (figure 4). This results in a negative sign for the Reynolds stress $\overline{u'w'}$, and consequently, the Stokes production term acts as a sink for turbulence kinetic energy. The dissipation and kelp drag dissipation terms are not shown for case B1R. The distribution of dissipation generally correlates with that of turbulence intensity, and strong kelp drag dissipation occurs where areas with high kelp frond density intersect with intense turbulence.

It is worthwhile noting that the originally farm-generated vertical shear has a comparable magnitude in cases B1R and B1H, e.g. near the farm leading edge in the range of x/h_b between 0 and 5 (figure 4). In fact, case B1R has even more pronounced sheared flow near the surface due to the existence of the dense layer. Nonetheless, the rapid

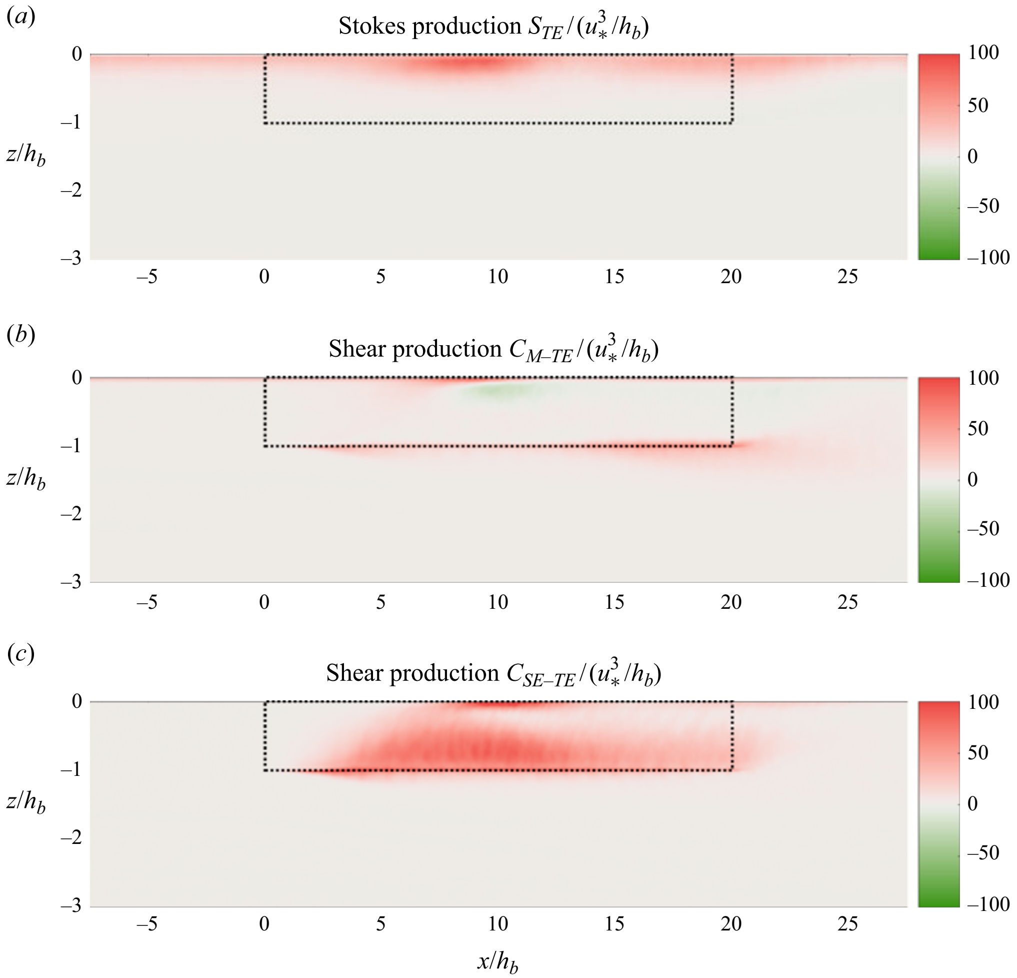

Figure 15. Side views of terms in the K_{TE} budget in (4.2c) for case S26H (rows aligned with the current, harvested profile). The results are temporally and laterally averaged. Dotted rectangles show the extent of the farm.

downstream increase in shear production in case B1H compared with B1R, e.g. for x/h_b from 5 to 15, indicates that its strength does not solely depend on the vertical shear induced by variations in frond area density. Instead, the increased Stokes production in case B1H plays a critical role in initiating the growth of turbulence and thus contributing to the enhancement of shear production. Further investigation of the distinct Stokes mechanisms in the two cases will be presented in § 5.

The turbulence kinetic energy budget is also evaluated for the case with laterally spaced rows (S26H, harvested profile). The distributions of Stokes production (figure 15), dissipation and canopy drag dissipation (not shown) are generally similar to those in the farm block case (B1H, harvested profile, figure 13), although with smaller magnitudes due to the overall lower effective density of the spaced rows. However, there is a distinction in shear production in the spaced rows as compared with the farm block, owing to the existence of secondary flow. Unlike the farm block case, where shear production directly converts mean flow energy to turbulence kinetic energy, a significant portion of turbulence

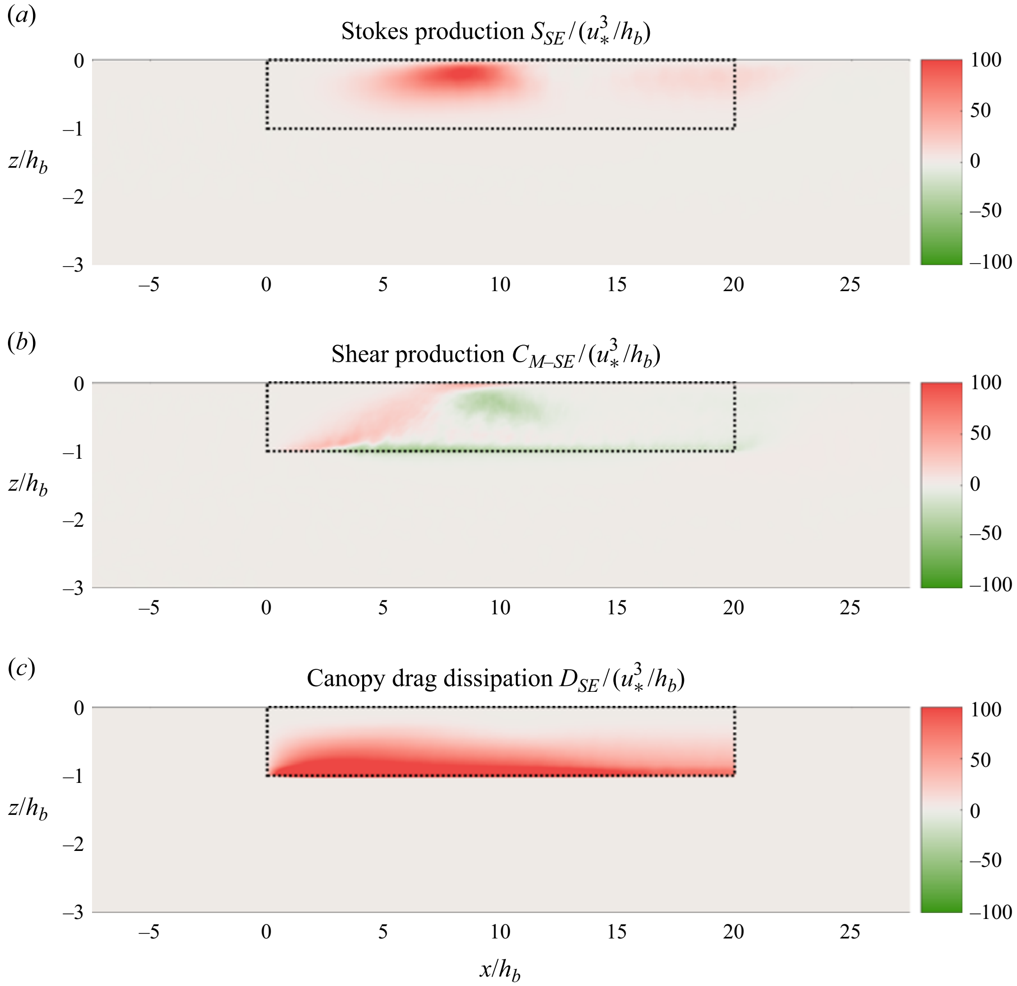

Figure 16. Side views of terms in the K_{SE} budget in (4.2*b*) for case S26H (rows aligned with the current, harvested profile). The results are temporally and laterally averaged. Dotted rectangles show the extent of the farm.

kinetic energy in spaced rows is generated through the conversion of secondary flow energy.

We subsequently calculate the secondary flow energy budget (figure 16). Note that the secondary flow energy encompasses both cross-stream variations in streamwise velocity ($\bar{u}^c$) and the steady lateral circulation ($\bar{v}^c$ and $\bar{w}^c$). Canopy dissipation D_{SE} is a significant source term in the secondary flow energy budget. Although the canopy drag leads to energy loss for both the mean flow and turbulence (hence named as a dissipation term), it can lead to a gain in secondary flow energy. This energy gain through D_{SE} is evident as cross-stream variations in the drag force, enhancing the cross-stream variability of streamwise flow. In addition, the Stokes production term is another major source of secondary flow energy, contributing to the generation of attached Langmuir circulation.

5. Vorticity dynamics of Langmuir circulations

The vorticity dynamics is investigated to understand the generation mechanisms of Langmuir circulation associated with various farm configurations. By manipulating the governing equations (2.1) and (2.2), we derive the transport equation for vorticity $\boldsymbol{\zeta}$ (e.g. Fujiwara, Yoshikawa & Matsumura 2018)

$$\frac{\partial \boldsymbol{\zeta}}{\partial t}+(\boldsymbol{u}\cdot\nabla)\boldsymbol{\zeta}+(\boldsymbol{u}_s\cdot\nabla)\boldsymbol{\zeta}=(\boldsymbol{\zeta}\cdot\nabla)\boldsymbol{u}+(\boldsymbol{\zeta}\cdot\nabla)\boldsymbol{u}_s-\nabla\times\boldsymbol{F}_D$$
$$+\nabla\times(\nabla\cdot\boldsymbol{\tau}^d)-\nabla\times\frac{\rho}{\rho_0}g\boldsymbol{e}_z+f\boldsymbol{e}_z\cdot\nabla(\boldsymbol{u}+\boldsymbol{u}_s). \tag{5.1}$$

The time derivative and advection terms are on the left-hand side. The first two terms on the right-hand side represent vorticity tilting and Stokes drift-vorticity tilting, respectively. The third term corresponds to the vorticity generation associated with canopy drag. The fourth to sixth terms represent the contributions of SGS stress, baroclinicity and rotation. For the sake of clarity, we express the equations for each vorticity component separately

$$\frac{\mathrm{D}\zeta_x}{\mathrm{D}t}=\zeta_x\frac{\partial u}{\partial x}+\zeta_y\frac{\partial u}{\partial y}+\zeta_z\frac{\partial u}{\partial z}+\zeta_z\frac{\partial u_s}{\partial z}+R_{\zeta,x}, \tag{5.2a}$$

$$\frac{\mathrm{D}\zeta_y}{\mathrm{D}t}=\zeta_x\frac{\partial v}{\partial x}+\zeta_y\frac{\partial v}{\partial y}+\zeta_z\frac{\partial v}{\partial z}-\frac{\partial F_{D,x}}{\partial z}+R_{\zeta,y}, \tag{5.2b}$$

$$\frac{\mathrm{D}\zeta_z}{\mathrm{D}t}=\zeta_x\frac{\partial w}{\partial x}+\zeta_y\frac{\partial w}{\partial y}+\zeta_z\frac{\partial w}{\partial z}+\frac{\partial F_{D,x}}{\partial y}+R_{\zeta,z}. \tag{5.2c}$$

The material derivative is defined as $\mathrm{D}/\mathrm{D}t=\partial/\partial t+\langle\overline{u_j}\rangle_y\partial/\partial x_j+u_s\partial/\partial x$, the same as (4.2). Note that we have assumed $F_{D,x}\gg F_{D,y}, F_{D,z}$, given that the streamwise velocity is much greater than lateral circulation, and we thus only focus on the influence of $F_{D,x}$ on vorticity. The term related to SGS stress diffuses vorticity rather than generating it; the baroclinic effect can be neglected because the farm is within the mixed layer; the effect of Earth's rotation is minimal. We thus group these factors into the residual terms, denoted as $R_{\zeta,x}$, $R_{\zeta,y}$ and $R_{\zeta,z}$.

The vorticity is calculated for case S26H (spaced kelp rows aligned with the current, harvested profile). Here, we introduce the phase average in the cross-stream direction, denoted as $\langle\cdot\rangle_p$, to average over equivalent positions of the periodically repeated rows. For any field ϕ, the cross-stream phase average is defined as

$$\langle\phi\rangle_p(x,y,z)=\frac{1}{N}\sum_{n=0}^{N-1}\phi\left(x,y+nS_{MF}+\frac{1}{2}W_{MF},z\right), \tag{5.3}$$

where N is the total number of rows.

The dominant phase-averaged terms in the vorticity equation are shown in figure 17. The persistent downstream vorticity ζ_x corresponds to the attached Langmuir circulation generated by kelp rows (recall figure 6*a*). The generation of attached Langmuir circulation is attributed to the tilting of vertical vorticity ζ_z by the Stokes drift into the downstream direction, i.e. the term $\zeta_z(\partial u_s/\partial z)$ in (5.2*a*). This tilting process aligns with the classical mechanism that gives rise to standard Langmuir circulation (e.g. Leibovich 1983). In the farm the vertical vorticity ζ_z is predominantly generated due to the drag discontinuity at the lateral edges of kelp rows, i.e. $\partial F_{D,x}/\partial y$ in (5.2*c*). The enhanced lateral shear in streamwise velocity (ζ_z) due to spaced kelp rows can thus lead to more intensified Langmuir circulation (ζ_x) within the farm (figures 17 and 18*a*), compared with the standard

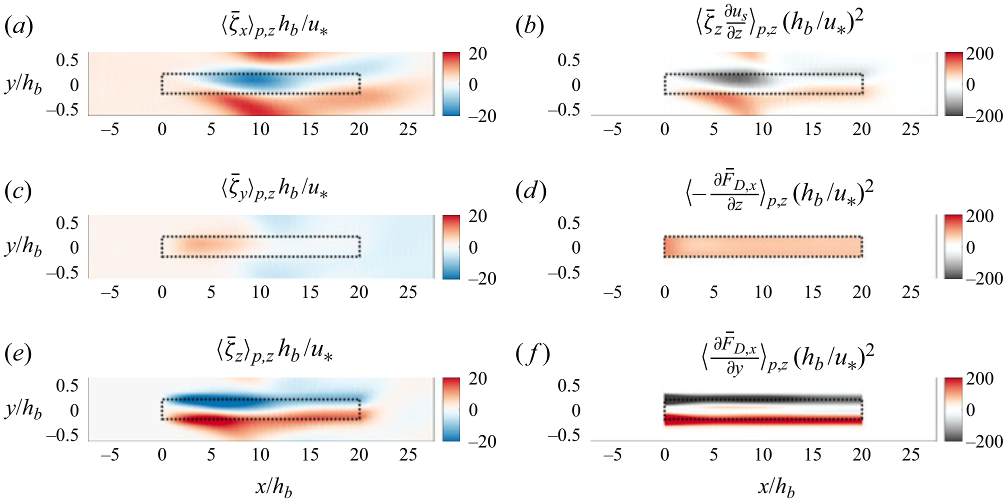

Figure 17. Top views of vorticity components ζ_x (*a*), ζ_y (*c*), ζ_z (*e*) and their primary forcing terms (*b*,*d*,*f*) in (5.2) for case S26H (rows aligned with the current, harvested profile). The results are time averaged, depth averaged ($z = 0$ to $-h_b$) and cross-phase averaged. Dotted rectangles show the extent of the kelp row.

Langmuir circulation upstream of the farm (Yan *et al.* 2021). Note that the vorticity field in figure 17 was averaged over time to show the persistent forcing and stationary Langmuir circulation associated with spaced kelp rows.

Subsequently, we investigate the vorticity dynamics in case B1H (farm block, harvested profile). Here, we analyse a representative snapshot as opposed to the time-averaged field, because the Langmuir circulation patterns in the farm block are transient and will be smeared out through time averaging. The strongest vorticity is generally aligned with the streamwise direction, i.e. the ζ_x component (figure 19*a*). This is particularly evident in regions of intensified Langmuir circulation, e.g. around x/h_b from 10 to 15 within the farm (comparing figure 19*a* with figure 6*b*). The pronounced ζ_x component is consistent with the feature of standard Langmuir circulation (McWilliams *et al.* 1997). The generation of ζ_x is primarily due to the vorticity tilting by the Stokes drift, i.e. $\zeta_z(\partial u_s/\partial z)$, similar to that in the kelp rows.

However, in contrast to the vorticity dynamics in the kelp rows, the influence of $\partial F_{D,x}/\partial y$ is diminished in the farm block due to the absence of lateral variations in kelp frond density. Instead, the vorticity generation is initiated from the leading edge of the farm block, where $\partial F_{D,x}/\partial z$, resulting from the vertical frond density variability, produces cross-stream vorticity ζ_y. The drag force is typically smaller near the surface for the harvested profile, which thus leads to a positive vertical shear with higher streamwise velocity on top of lower velocity, i.e. positive ζ_y (figure 19*c*). The higher streamwise velocity near the surface tends to concentrate toward regions with surface convergence (indicative of downwelling), as a result of lateral and vertical advection by Langmuir circulation. Similarly, lower streamwise velocity is transported to the upwelling regions in the cross-section. The associated lateral variability in streamwise velocity enhances vertical vorticity ζ_z (figure 19*e*), which can subsequently be tilted into ζ_x by the Stokes drift (figure 19*a*). The increased ζ_x represents stronger Langmuir circulation that can further interact with the other vorticity components ζ_y and ζ_z. This interaction leads to positive feedback, thereby intensifying Langmuir circulation.

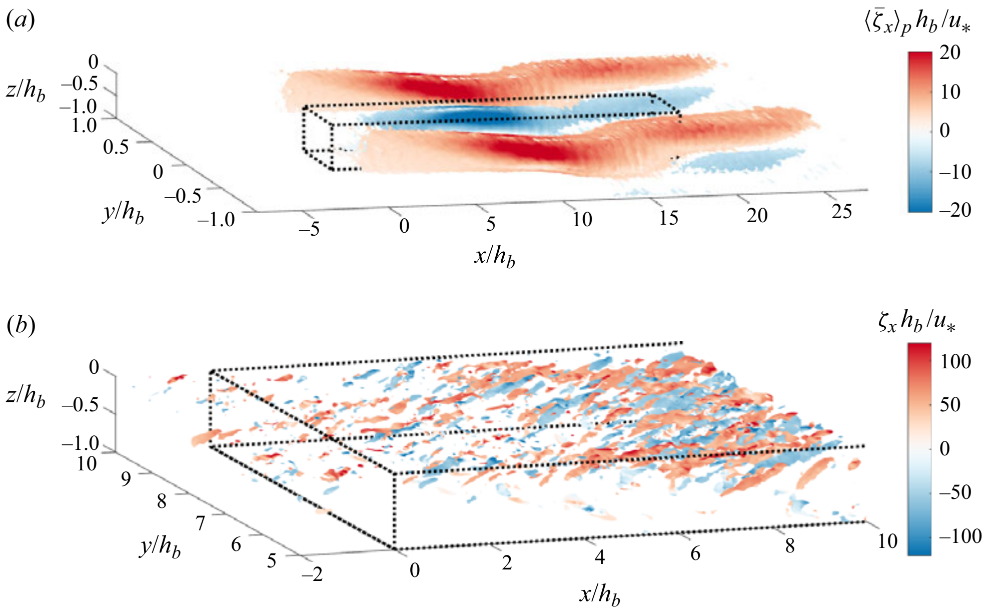

Figure 18. Three-dimensional representation of vortex structures, as revealed by isosurfaces of λ_2. (*a*) Cross-phase-averaged and time-averaged streamwise vorticity $\langle\bar{\zeta}_x\rangle_p$ for a kelp row in case S26H (rows aligned with the current, harvested profile). (*b*) A zoom-in view of the instantaneous streamwise vorticity ζ_x for case B1H (farm block, harvested profile). Note the differences in colour map range and axis range between the two plots.

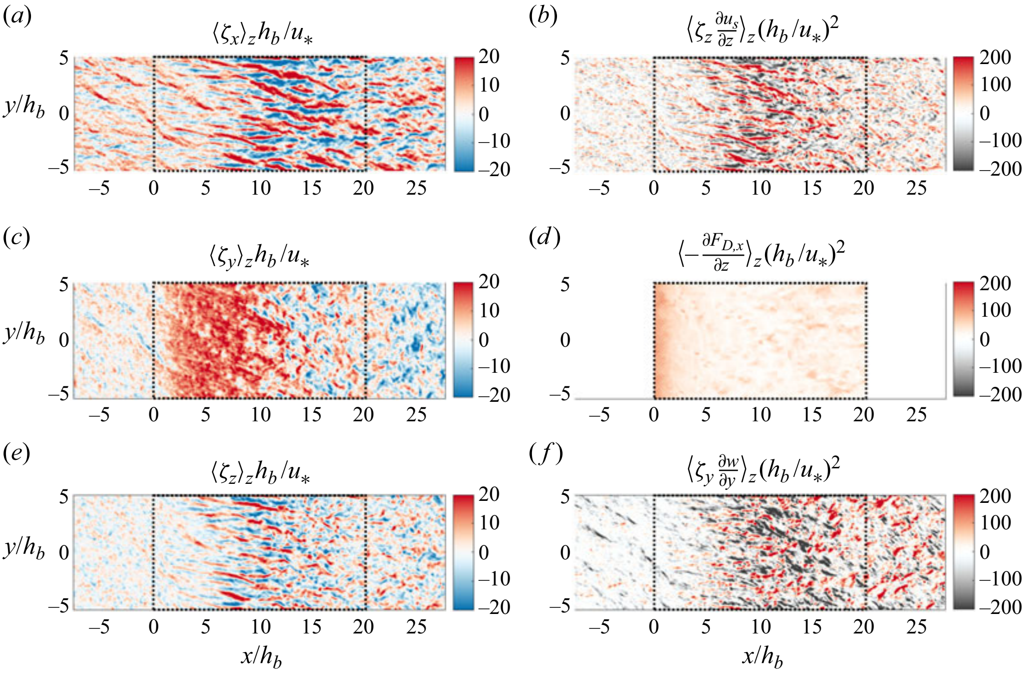

Figure 19. Top views of vorticity components ζ_x (*a*), ζ_y (*c*), ζ_z (*e*) and their primary forcing terms (*b*,*d*,*f*) in (5.2) for case B1H (farm block, harvested profile). The results are snapshots of depth-averaged ($z = 0$ to $-h_b$) results. Dotted rectangles show the extent of the farm.

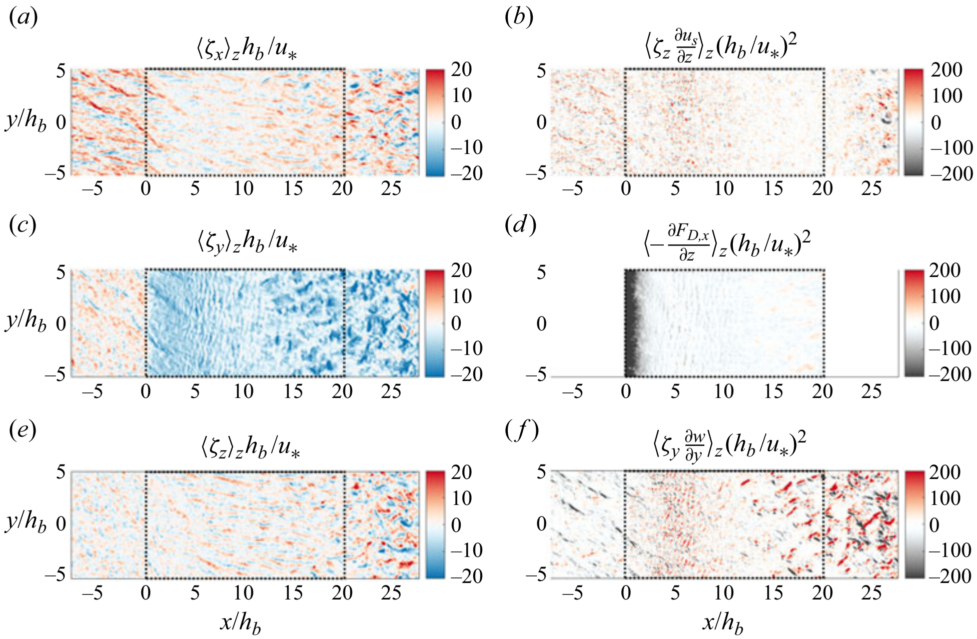

Figure 20. Top views of vorticity components ζ_x (*a*), ζ_y (*c*), ζ_z (*e*) and forcing terms (*b*,*d*,*f*) in (5.2) for case B1R (farm block, ripe profile). These are snapshots of depth-averaged ($z = 0$ to $-h_b$) results. Dotted rectangles show the extent of the farm.

The processes described above are consistent with the CL2 mechanism (Craik 1977; Leibovich 1977, 1983), which is widely recognized as a key driving factor for standard Langmuir circulation. According to the CL2 mechanism, the vorticity tilting due to Stokes drift can cause instability and produce Langmuir circulation cells when the vertical shear of the Eulerian wind-driven current is in the same direction as the vertically sheared Stokes drift. In our study, the presence of the kelp farm further enhances the vertical shear in the OML through the vertical variability of canopy drag, thus promoting the growth of instability and leading to more intensified Langmuir circulation.

Note that the patterns of ζ_y and ζ_z are generally consistent with the forcing terms $\partial F_{D,x}/\partial z$ and $\zeta_y(\partial w/\partial y)$ in the upstream region of the farm, where these vorticity components are initially generated (figure 19). Other vorticity tilting terms become more prominent as Langmuir circulation is rapidly enhanced downstream. This leads to the more complex vorticity patterns found in the downstream part of the farm.

In contrast, in the farm block with the ripe profile (case B1R), the presence of the dense layer near the surface tends to decelerate the streamwise current. Consequently, negative vertical shear arises with lower streamwise velocity on top of higher velocity, in particular near the sea surface where the Stokes drift shear is most pronounced (figure 4*a*). This leads to the negative depth-averaged ζ_y in figure 20(*c*), in contrast to the positive ζ_y in figure 19(*c*) associated with the harvested profile (case B1H). The negative vertical shear due to the ripe profile in case B1R results in a scenario that suppresses the growth of CL2 instability. It thus explains the weak vorticity and absence of Langmuir circulation patterns in the farm block with the ripe profile (figures 20 and 6*c*).

Furthermore, we examine the streamwise evolution of different vorticity components. In the farm block with the ripe profile (case B1R), cross-stream vorticity ζ_y promptly

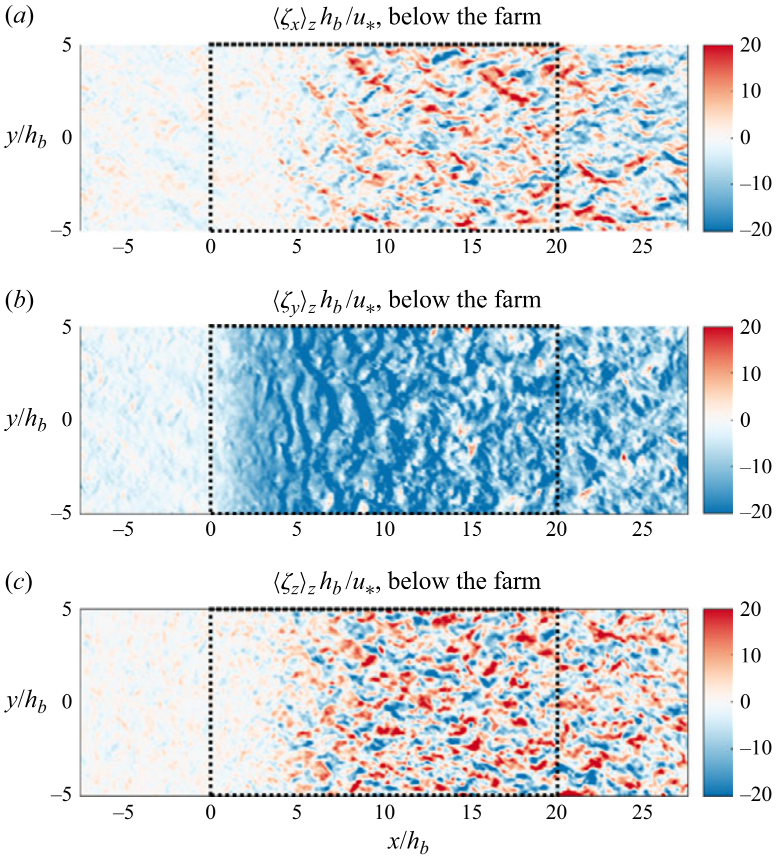

Figure 21. Top views of vorticity components ζ_x (*a*), ζ_y (*b*) and ζ_z (*c*) for case B1H (farm block, harvested profile). These are snapshots of depth-averaged ($z = -h_b$ to $-2h_b$) results below the farm. Dotted rectangles show the extent of the farm.

increases at the leading edge driven by the canopy drag gradient $\partial F_{D,x}/\partial z$. Downstream of the leading edge, all the vorticity components tend to diminish in magnitude through the farm due to the lack of Langmuir circulation generation. In the farm block with the harvested profile (case B1H), the rapid growth of ζ_y at the leading edge subsequently causes the increase of ζ_z and ζ_x, as a result of the tilting mechanism. In comparison, within the spaced kelp rows (case S26H), the vertical vorticity ζ_z is the vorticity component that initially increases, driven by $\partial F_{D,x}/\partial y$ at the lateral edges of kelp rows, and this increase in ζ_z is followed by the intensification of ζ_x and ζ_y. This contrast again demonstrates the distinction in vorticity generation mechanisms between the two farm configurations. It also elucidates why Langmuir turbulence still occurs in kelp rows aligned with the current even with the ripe profile (e.g. case S26R): ζ_z can be persistently generated by the spaced kelp rows and then tilted by the Stokes drift to produce ζ_x, even if a vertical shear that favours the CL2 mechanism is not created.

Differing from the Langmuir patterns found within the farm, the vorticity patterns beneath the farm generally resemble the classical shear layer turbulence (Finnigan, Shaw & Patton 2009; Bailey & Stoll 2016) (figure 21). Negative cross-stream vorticity ζ_y is generated due to the drag discontinuity ($\partial F_{D,x}/\partial z$) at the canopy bottom edge.

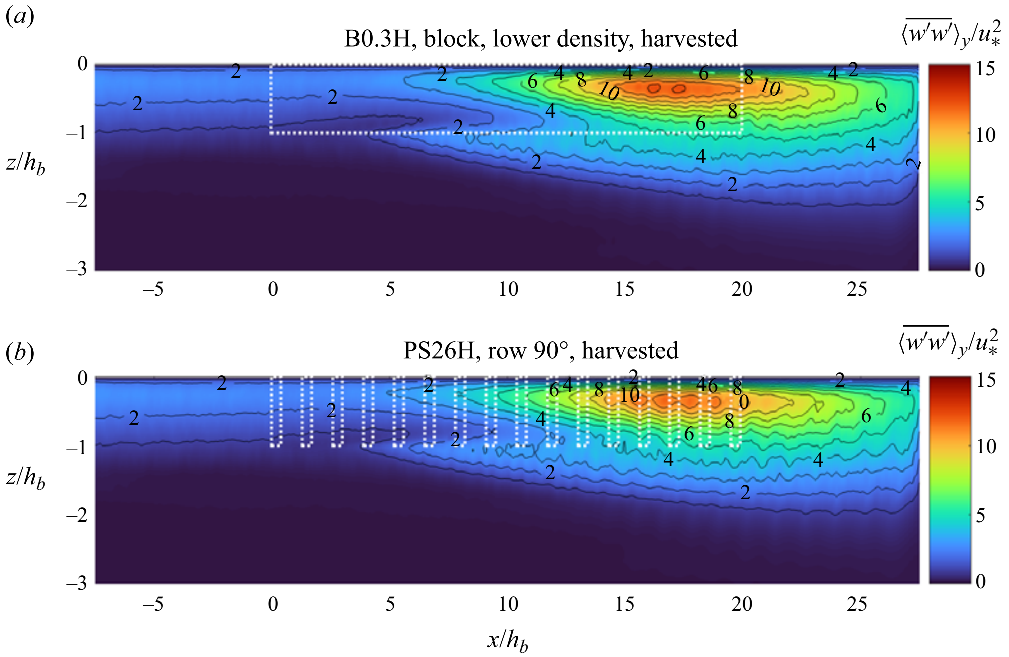

Figure 22. Side views of the transient component of vertical velocity variance $\langle \overline{w'w'} \rangle_y / u_*^2$. (*a*) Case B0.3H, farm block with a lower frond area density, harvested profile. (*b*) Case PS26H, spaced rows oriented perpendicular to the geostrophic current, harvested profile. The results are temporally and laterally averaged, similar to figure 7. Dotted rectangles show the extent of the farm block or rows. Note that cases B0.3H and PS26H have an equal effective density $\langle a \rangle_{xyz}$.

Other vorticity components ζ_x and ζ_z subsequently increase as a result of vorticity tilting. The influence of Stokes drift rapidly diminishes with depth, and the Stokes drift–vorticity tilting term is thus negligible below the farm.

6. Sensitivity to other farm parameters

6.1. *Effective density*

In the previous sections, we focused on distinctions between farm blocks and spaced rows and between different vertical frond density profiles. In addition, the farm effective density is also a key characteristic affecting the hydrodynamics of suspended farms (Poggi *et al.* 2004; Belcher *et al.* 2012; Bailey & Stoll 2013). Figure 22(*a*) shows the turbulence kinetic energy in the farm block with a lower effective density $\langle a \rangle_{xyz}$ (case B0.3H, harvested profile, with a density lower than case B1H by a factor of 0.3). Overall, the shear layer turbulence below the canopy is weaker in case B0.3H compared with B1H, consistent with the expected dependence on effective density for classical canopy flow (Poggi *et al.* 2004; Bailey & Stoll 2013).

Turbulence intensity within the canopy typically decreases with the increased effective density $\langle a \rangle_{xyz}$ for classical canopy flow without waves. This is because a higher effective density reduces the penetration of shear layer turbulence into the canopy and also enhances the dissipation of turbulence by canopy drag. However, in our study turbulence is weaker in the lower-density farm block compared with the higher-density case (figures 22*a* and 7*b*).

This is because the lower density leads to weaker shear (or vorticity) in the canopy, and thus a weaker Stokes drift–vorticity tilting mechanism and less Langmuir turbulence production (§§ 4 and 5).

Moreover, the region with maximum Langmuir turbulence intensity occurs at a larger downstream distance from the farm leading edge in the lower effective density case compared with the higher-density case. This is because it takes a longer distance for flow to adjust to canopy drag and for shear to develop with a lower effective density. This longer development distance is consistent with (3.4), where the adjustment length is expected to be inversely proportional to the effective density.

6.2. *Farm orientation*

The dependence of turbulence generation on farm orientation is also examined through a set of simulations with kelp rows oriented perpendicular to the direction of current and waves (cases ‘PS’). This is particularly relevant to the farm design problem in realistic ocean environments, given the variability of submesoscale processes. Farms with kelp rows perpendicular to the flow generally behave similarly to farm blocks that have an identical effective density $\langle a\rangle_{xyz}$, e.g. case PS26H in figure 22(*b*) and case B0.3H in figure 22(*a*), both of which have a same effective density of $0.35\,\mathrm{m}^{-1}$. Note that the configuration with spaced rows could lead to additional stationary streamwise deviations in canopy flow, typically corresponding to a dispersive flux (Bailey & Stoll 2013; Li & Bou-Zeid 2019). Nevertheless, the influences of dispersive processes appear to be minimal in the examined cases, and the statistics of kelp rows perpendicular to the flow are broadly similar to uniform farm blocks (figure 5).

6.3. *Synthesis*

We have presented cases B0.3H and PS26H (refer to table 1) above as a representative to illustrate the impacts of effective density and farm orientation. Other simulations with various density or farm configurations generally show a consistent dependence on effective density $\langle a\rangle_{xyz}$. As has been summarized in figure 5(*d*), the intensity of shear layer turbulence below the farm positively depends on the effective density for all the simulations. In addition, for cases with the harvested profile, which favours the generation of Langmuir-type turbulence, turbulence intensity within the farm increases as the effective density is increased (figure 5*a*).

By contrast, for the ripe profile, no obvious dependence of within-farm turbulence intensity on the effective density is found for farm blocks and kelp rows oriented perpendicular to the flow (figure 5*a*), because of the absence of Langmuir circulation. For kelp rows aligned with the geostrophic flow with the ripe profile, turbulence intensity asymptotes toward a farm block scenario or no farm scenario with either increasing or decreasing effective density, and the maximum intensity is achieved with an effective density of around $0.5\,\mathrm{m}^{-1}$.

The distance for farm-generated Langmuir turbulence to peak generally increases with the decreased effective density $\langle a\rangle_{xyz}$, for configurations with a farm block or kelp rows perpendicular to flow. Nevertheless, in kelp rows aligned with flow, the distance for Langmuir turbulence to develop is much smaller than a farm block with an identical effective density, e.g. comparing figure 7(*a*) with figure 22(*a*). This is because kelp rows aligned with the current can lead to rapid growth of Langmuir turbulence through the creation of vorticity at lateral edges of rows by the drag force gradient $\partial F_{D,x}/\partial y$. It further

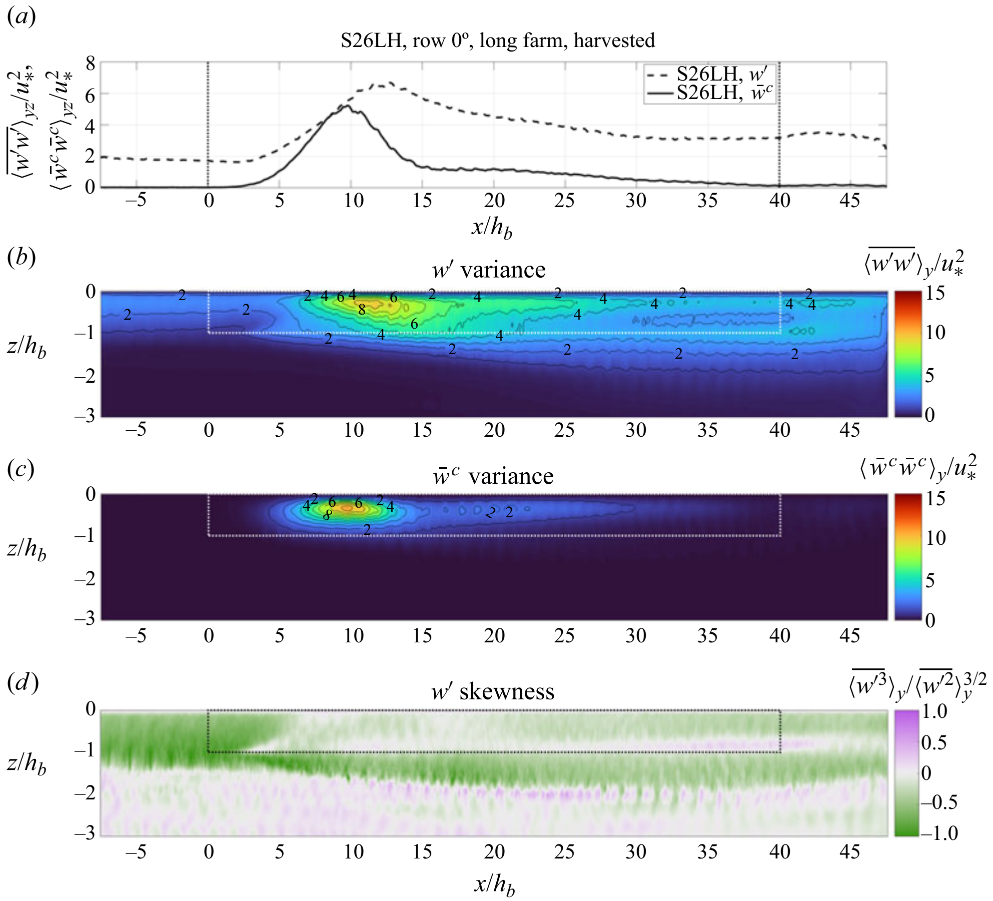

Figure 23. Turbulence and secondary flow statistics in the long farm simulation (case S26LH, spaced rows aligned with the current, harvested profile). (*a*) Streamwise variations of vertical velocity variance $\langle\overline{w'w'}\rangle_y/u_*^2$ (turbulence component, dashed line) and $\langle\bar{w}^c\bar{w}^c\rangle_y/u_*^2$ (secondary flow component, solid line). The results are temporally, laterally and vertically ($z = 0$ to $-h_b$) averaged. Vertical dotted lines show the extent of the farm. Panels (*b*) and (*c*) show side views of $\langle\overline{w'w'}\rangle_y/u_*^2$ and $\langle\bar{w}^c\bar{w}^c\rangle_y/u_*^2$. The results are temporally and laterally averaged. Dotted rectangles show the extent of the farm. (*d*) Side view of the skewness of w'.

implies that this type of configuration may result in a shorter adjustment region length compared with that expected with the effective density in (3.4).

6.4. *Extended farm length*

We ran an additional simulation (case S26LH, refer to table 1) with an extended farm length of $L_{MF} = 800\,\text{m}$ to further investigate the downstream development of farm-generated turbulence. The long farm case S26LH has the same configuration as case S26H (spaced kelp rows aligned with the flow with $S_{MF} = 26\,\text{m}$, harvested profile). The turbulence and secondary flow characteristics in the upstream part of the long farm are generally similar to that of the short farm, e.g. comparing figure 23 with figures 7(*a*), 8 and 11(*a*).

In the upstream part of the long farm, secondary flow diminishes after around $x/h_b = 15$, and turbulence intensity also remains at a stable value after a decay from its peak value (figure 23*a*,*b*). Turbulence statistics near the trailing edge of the long farm are broadly similar to those of another simulation with an infinite farm length (not shown). The canopy flow is thus considered as having reached an equilibrium state toward the long farm trailing edge.

We note that the farm-generated Langmuir-type turbulence and secondary flow investigated in this study primarily occurs in the upstream part of the farm where flow is adapting to the canopy drag, before the establishment of an equilibrium canopy flow. Nevertheless, our investigation is relevant to the farm design problem, given that the farm length is comparable to or less than the canopy adjustment length in a range of realistic farm design considerations.

The turbulence intensity near the long farm trailing edge, in spite of the disappearance of secondary flow there, is still higher than that of the standard Langmuir turbulence observed upstream of the farm (figure 23*a*). Moreover, it is worthwhile noting that positive skewness of w' only occurs in the lower one third of the canopy in the equilibrium state at the trailing edge (figure 23*d*). The positive skewness of w' is a typical feature of the shear layer turbulence that penetrates into the canopy, corresponding to the prevalent presence of sweep events (Raupach & Thom 1981; Katul *et al.* 1997; Poggi *et al.* 2004). The negative skewness of w' above the penetrated shear layer is indicative of the Langmuir-type turbulence (McWilliams *et al.* 1997). This indicates that the shear layer turbulence growing from the farm bottom does not penetrate through the entire canopy in the equilibrium state.

We calculate the penetration length scale δ_e based on the empirical relationship (Nepf *et al.* 2007; Nepf & Ghisalberti 2008)

$$\delta_e = \frac{0.23}{\dfrac{1}{2} C_D \langle a \rangle_{xyz}}. \tag{6.1}$$

Here, the factor of $\frac{1}{2}$ accounts for the projection of frond surface area (term $\boldsymbol{P}$ in (2.5)). The calculated δ_e is four times larger than the canopy height, suggesting that shear layer eddies would penetrate to the sea surface in fully developed canopy flow. As a comparison, in the simulation without waves (case S26H-NW), positive skewness of w', which represents shear layer turbulence, occupies the entire farm height after around $x/h_b = 15$, and this is consistent with the prediction from (6.1). Nevertheless, the coexistence of both positive and negative skewness of w' in figure 23(*d*) implies that wave effects can impede the penetration of shear layer eddies. An adjusted OML is established in the equilibrium state, characterized by a combination of Langmuir-type turbulence and penetrated shear layer turbulence.

7. Conclusion

In this study, we investigate the influence of various suspended farm configurations on the OML hydrodynamics. The drag force induced by kelp can alter the vertical profile of mean flow and leads to generation of shear layer turbulence beneath the farm. Moreover, Langmuir circulation can be generated within the farm, differing from the standard Langmuir circulation in the absence of a farm. These modifications to the OML depend on both the farm horizontal arrangement and the vertical profile of frond area density.

In farm blocks or spaced kelp rows that are perpendicular to the current, distinctions in Langmuir circulation patterns emerge between the harvested profile and ripe profile (without and with the dense layer near the surface, respectively). Enhanced Langmuir circulation occurs in the farm with the harvested profile, characterized by transient patterns that have a larger magnitude compared with the standard Langmuir circulation upstream of the farm. The average turbulence intensity in the farm, dominantly contributed by Langmuir turbulence, has a positive dependence on the effective density $\langle a\rangle_{xyz}$. The generation of Langmuir turbulence is attributed to the establishment of a vertically sheared current profile that favours CL2 instability, as a result of the vertical variability in canopy drag. The lateral vorticity (vertical shear of streamwise velocity) gives rise to vertical vorticity, which is subsequently tilted into streamwise vorticity by the Stokes drift to create Langmuir circulation. By contrast, for the ripe profile, a reversed vertical shear occurs near the sea surface due to the presence of the dense kelp layer, and Langmuir turbulence is absent in the farm due to the suppression of CL2 instability.

The farm configuration involving spaced kelp rows aligned with the flow leads to the generation of attached Langmuir circulation for both the harvested and ripe profiles. The attached Langmuir circulation is spatially locked in the lateral direction, comprising both a turbulence component and a stationary secondary flow component. Strong lateral shear is generated at the lateral edges of kelp rows, and this vertical vorticity is subsequently tilted into the streamwise direction by the Stokes drift, producing attached Langmuir circulation. The intensity of Langmuir turbulence monotonically increases with the effective density $\langle a\rangle_{xyz}$ for the harvested profile. However, for the ripe profile, the enhancement of Langmuir turbulence diminishes at either high $\langle a\rangle_{xyz}$, resembling a farm block, or low $\langle a\rangle_{xyz}$, resembling a scenario without a farm. The peak value occurs at an intermediate effective density, which is around $\langle a\rangle_{xyz} = 0.5\,\mathrm{m}^{-1}$ in our simulations. Additionally, the strength of the secondary flow increases from the kelp row lateral spacing S_{MF} of 13 m to 52 m, and decays at $S_{MF} = 208$ m. The simulations do not allow for an accurate determination of the maximum secondary flow intensity with respect to S_{MF}, and it appears to fall within the range of $S_{MF} = 52$ m and 208 m.

The vertical shear of mean flow is enhanced below the farm, leading to development of shear layer turbulence. The intensity of shear layer turbulence generally increases with the effective density $\langle a\rangle_{xyz}$, while displaying a minimal dependence on the specific farm configuration.

We have focused on a specific set of representative oceanic conditions in the present study, and the implications of turbulence generation can be extended to various wave and current conditions. Stronger winds and waves typically increase the Stokes drift and the CL vortex force, therefore further intensifying Langmuir turbulence within the farm configurations that favour turbulence generation. Weaker ocean currents would lead to a reduced level of shear layer turbulence below the farm, as its generation depends on the magnitude of shear (figure 5*d*,*e*). Moreover, the enhancement of Langmuir turbulence in the farm relies on the interaction between the Stokes drift and farm-modulated currents. The canopy drag effect would diminish under conditions of weaker ocean currents, which is thus expected to result in less deviation from the standard Langmuir turbulence.

The different mean flow, secondary flow and turbulence characteristics associated with various farm configurations have significant implications for nutrient transport and farm performance, as will be examined in an upcoming companion study. Moreover, the presence of suspended farms notably alters the turbulence intensity within the OML. These findings underscore the potential of floating obstacle structures in reshaping characteristics of the ocean surface boundary layer. The presence of such floating structures may enhance the shear in ocean currents, giving rise to shear layer turbulence. Additionally, the modified velocity profile caused by floating structures can interact with surface gravity waves, thereby influencing the generation of Langmuir turbulence in the OML.

Case	Wave	L_{MF} (m)	S_{MF} (m)	W_{MF} (m)	Frond vert. prof.	Orientation	$\langle a \rangle_{xyz}$ (m^{-1})
B1H ⋆	Yes	400	—	208	Harvested	—	1.14
B0.3H	Yes	400	—	208	Harvested	—	0.35
B0.16H	Yes	400	—	208	Harvested	—	0.18
B0.08H	Yes	400	—	208	Harvested	—	0.09
B1R ⋆	Yes	400	—	208	Ripe	—	2.20
B0.3R	Yes	400	—	208	Ripe	—	0.68
B0.16R	Yes	400	—	208	Ripe	—	0.35
B0.08R	Yes	400	—	208	Ripe	—	0.18
S26H ⋆	Yes	400	26	8	Harvested	Aligned	0.35
S13H	Yes	400	12	8	Harvested	Aligned	0.70
S16H	Yes	400	16	8	Harvested	Aligned	0.57
S52H	Yes	400	52	8	Harvested	Aligned	0.18
S52W20H	Yes	400	52	20	Harvested	Aligned	0.44
S208H	Yes	400	208	8	Harvested	Aligned	0.04
S26R	Yes	400	26	8	Ripe	Aligned	0.67
S13R	Yes	400	13	8	Ripe	Aligned	1.35
S16R	Yes	400	16	8	Ripe	Aligned	1.10
S52R	Yes	400	52	8	Ripe	Aligned	0.34
S52W20R	Yes	400	52	20	Ripe	Aligned	0.85
S208R	Yes	400	208	8	Ripe	Aligned	0.08
S26LH	Yes	800	26	8	Harvested	Aligned	0.35
PS26H	Yes	400	26	8	Harvested	Perpendicular	0.35
PS52H	Yes	400	52	8	Harvested	Perpendicular	0.18
PS52W20H	Yes	400	52	20	Harvested	Perpendicular	0.44
PS26R	Yes	400	26	8	Ripe	Perpendicular	0.67
PS52R	Yes	400	52	8	Ripe	Perpendicular	0.34
PS52W20R	Yes	400	52	20	Ripe	Perpendicular	0.85
PRE	Yes	—	—	—	—	—	—
B1H-NW	No	400	—	208	Harvested	—	1.14
B1R-NW	No	400	—	208	Ripe	—	2.20
S26H-NW	No	400	26	8	Harvested	Aligned	0.35
PRE-NW	No	—	—	—	—	—	—

Table 1. Farm parameters. The cases selected for detailed analysis are marked with stars. The letters ‘H’ and ‘R’ denote harvested and ripe profiles, respectively. The letter ‘B’ represents farm block cases, and 1, 0.3, 0.16 and 0.08 are the frond density multiplication factors, influencing the effective density $\langle a \rangle_{xyz}$. The letter ‘S’ represents spaced kelp rows aligned with the x-direction, and ‘PS’ represents spaced kelp rows oriented perpendicular to the x-direction. Numeric values 13, 16, 26, 52 and 208 denote the row spacing parameter (S_{MF}, in metres). Most configurations have a row width W_{MF} of 8 m, and several cases have a row width of 20 m, denoted by ‘W20’. Additionally, a long farm simulation is named as S26LH, characterized by an extended farm length L_{MF} of 800 m. The precursor simulation in absence of a farm is referred to as PRE. The term ‘−NW’ is used to denote the simulations conducted without any surface wave forcing, meaning the Stokes drift velocity is zero.

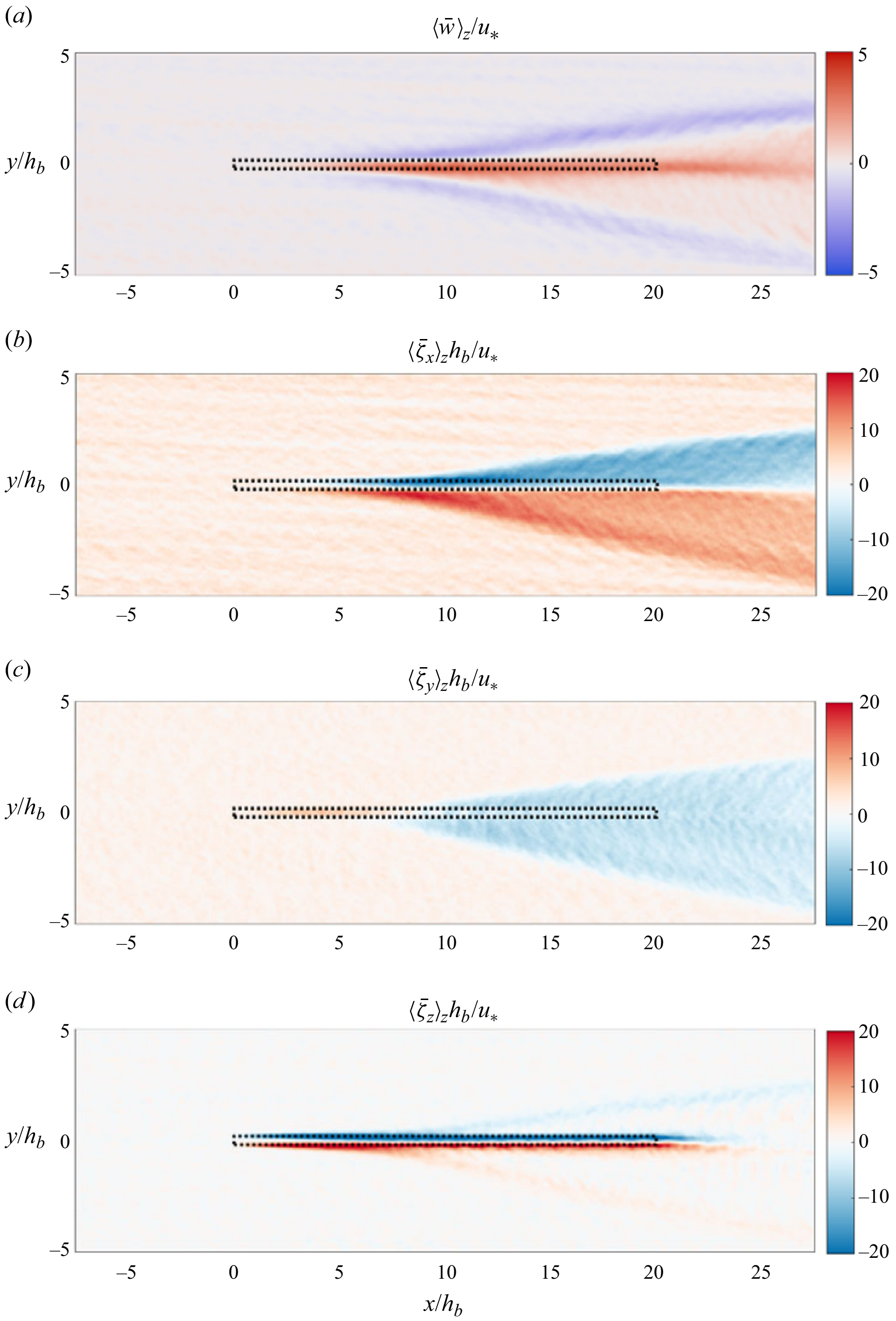

Figure 24. Top views of vertical velocity w (a) and vorticity components ζ_x, ζ_y and ζ_z (b–d) for case S208H (a single row aligned with the current, harvested profile). These results are time averaged and depth averaged ($z = 0$ to $-h_b$). Dotted rectangles show the extent of the kelp row.

Acknowledgements. The authors thank K. Davis for helpful discussions. Suggestions and comments provided by two anonymous reviewers are greatly appreciated.

Funding. The research leading to these results was funded by the ARPA-E MARINER Program DE-AR0000920. We would like to acknowledge high-performance computing support from Cheyenne (doi:10.5065/D6RX99HX) provided by NCAR's Computational and Information Systems Laboratory, sponsored by the National Science Foundation. C.Y. is supported by the youth innovation team of China Meteorological Administration (no. CMA2024QN14).

Declaration of interests. The authors report no conflict of interest.

Author ORCIDs.
Tong Bo https://orcid.org/0000-0002-6030-0561;
James C. McWilliams https://orcid.org/0000-0002-1237-5008;
Chao Yan https://orcid.org/0000-0001-6708-5465;
Marcelo Chamecki https://orcid.org/0000-0003-0576-0597.

Appendix A. Detailed farm parameters

A range of farm simulations with spaced rows are conducted (table 1), where the spacing parameter S_{MF} varies from 13 to 208 m. The kelp row width is $W_{MF} = 8$ m for different S_{MF}. There is also an additional case with an increased row width of $W_{MF} = 20$ m for $S_{MF} = 52$ m. We primarily focus on cases with the farm length of $L_{MF} = 400$ m, and a long farm simulation with $L_{MF} = 800$ m is also investigated for $S_{MF} = 26$ m and $W_{MF} = 8$ m.

For farm block simulations, each frond density profile is additionally multiplied by a factor of 0.3, 0.16 or 0.08, to investigate the influence of decreased effective density (table 1). Note that the kelp farm block simulations with a multiplication factor of 0.3 or 0.16 result in an identical effective density $\langle a\rangle_{xyz}$ to the spaced kelp row simulations with $S_{MF} = 26$ m or $S_{MF} = 52$ m, respectively, for a row width of $W_{MF} = 8$ m.

Appendix B. A single kelp row

Figure 24 shows the simulation of a single kelp row aligned with the current and waves (case S208H, harvested profile, corresponding to a lateral spacing S_{MF} of 208 m under periodic boundary conditions in y-direction). The regions with strong farm-generated vertical vorticity ζ_z remain close to the lateral edges of the kelp row. The vertical velocity w and streamwise vorticity ζ_x, which correspond to the attached Langmuir circulation, exhibit a downstream expansion in width. This lateral expansion of Langmuir circulation, i.e. the Langmuir wake pattern associated with the farm, can thus influence the horizontal distribution of farm-generated turbulence and secondary flow. Moreover, in kelp rows with smaller lateral spacing S_{MF}, the expansion of the wake may encounter interference due to the presence of other neighbouring rows.

REFERENCES

Bailey, B.N. & Stoll, R. 2013 Turbulence in sparse, organized vegetative canopies: a large-eddy simulation study. *Boundary-Layer Meteorol.* **147**, 369–400.

Bailey, B.N. & Stoll, R. 2016 The creation and evolution of coherent structures in plant canopy flows and their role in turbulent transport. *J. Fluid Mech.* **789**, 425–460.

Belcher, S.E., Harman, I.N. & Finnigan, J.J. 2012 The wind in the willows: flows in forest canopies in complex terrain. *Annu. Rev. Fluid Mech.* **44**, 479–504.

Belcher, S.E., Jerram, N. & Hunt, J.C.R. 2003 Adjustment of a turbulent boundary layer to a canopy of roughness elements. *J. Fluid Mech.* **488**, 369–398.

BOU-ZEID, E., MENEVEAU, C. & PARLANGE, M. 2005 A scale-dependent Lagrangian dynamic model for large eddy simulation of complex turbulent flows. *Phys. Fluids* **17** (2), 025105.

CHAMECKI, M., CHOR, T., YANG, D. & MENEVEAU, C. 2019 Material transport in the ocean mixed layer: recent developments enabled by large eddy simulations. *Rev. Geophys.* **57** (4), 1338–1371.

CHARRIER, B., WICHARD, T. & REDDY, C.R.K. 2018 *Protocols for Macroalgae Research*. CRC.

CHOR, T., MCWILLIAMS, J.C. & CHAMECKI, M. 2020 Diffusive–nondiffusive flux decompositions in atmospheric boundary layers. *J. Atmos. Sci.* **77** (10), 3479–3494.

CHOR, T., MCWILLIAMS, J.C. & CHAMECKI, M. 2021 Modifications to the k-profile parameterization with nondiffusive fluxes for Langmuir turbulence. *J. Phys. Oceanogr.* **51** (5), 1503–1521.

CHURCHFIELD, M.J., LEE, S., MICHALAKES, J. & MORIARTY, P.J. 2012 A numerical study of the effects of atmospheric and wake turbulence on wind turbine dynamics. *J. Turbul.* **13**, N14.

CRAIK, A.D.D. 1977 The generation of Langmuir circulations by an instability mechanism. *J. Fluid Mech.* **81** (2), 209–223.

CRAIK, A.D.D. & LEIBOVICH, S. 1976 A rational model for Langmuir circulations. *J. Fluid Mech.* **73** (3), 401–426.

DAYTON, P.K. 1985 Ecology of kelp communities. *Annu. Rev. Ecol. Syst.* **16** (1), 215–245.

DIERSSEN, H.M., ZIMMERMAN, R.C., DRAKE, L.A. & BURDIGE, D.J. 2009 Potential export of unattached benthic macroalgae to the deep sea through wind-driven Langmuir circulation. *Geophys. Res. Lett.* **36** (4), L04602.

EVANS, G.T. & TAYLOR, F.J.R. 1980 Phytoplankton accumulation in Langmuir cells 1. *Limnol. Oceanogr.* **25** (5), 840–845.

FERDOUSE, F., HOLDT, S.L., SMITH, R., MURÚA, P. & YANG, Z. 2018 The global status of seaweed production, trade and utilization. *Glob. Res. Programme* **124**, 120.

FINNIGAN, J. 2000 Turbulence in plant canopies. *Annu. Rev. Fluid Mech.* **32** (1), 519–571.

FINNIGAN, J.J., SHAW, R.H. & PATTON, E.G. 2009 Turbulence structure above a vegetation canopy. *J. Fluid Mech.* **637**, 387–424.

FRIEDER, C.A., *et al.* 2022 A macroalgal cultivation modeling system (MACMODS): evaluating the role of physical-biological coupling on nutrients and farm yield. *Front. Mar. Sci.* **9**, 752951.

FUJIWARA, Y., YOSHIKAWA, Y. & MATSUMURA, Y. 2018 A wave-resolving simulation of Langmuir circulations with a nonhydrostatic free-surface model: comparison with Craik–Leibovich theory and an alternative Eulerian view of the driving mechanism. *J. Phys. Oceanogr.* **48** (8), 1691–1708.

GHADIRYANFAR, M., ROSENTRATER, K.A., KEYHANI, A. & OMID, M. 2016 A review of macroalgae production, with potential applications in biofuels and bioenergy. *Renew. Sust. Energy Rev.* **54**, 473–481.

JACKSON, G.A. 1997 Currents in the high drag environment of a coastal kelp stand off California. *Cont. Shelf Res.* **17** (15), 1913–1928.

KARA, A.B., ROCHFORD, P.A. & HURLBURT, H.E. 2000 An optimal definition for ocean mixed layer depth. *J. Geophys. Res.* **105** (C7), 16803–16821.

KATUL, G., KUHN, G., SCHIELDGE, J. & HSIEH, C.-I. 1997 The ejection-sweep character of scalar fluxes in the unstable surface layer. *Boundary-Layer Meteorol.* **83**, 1–26.

KOEHL, M.A.R. & WAINWRIGHT, S.A. 1977 Mechanical adaptations of a giant kelp. *Limnol. Oceanogr.* **22** (6), 1067–1071.

LANGMUIR, I. 1938 Surface motion of water induced by wind. *Science* **87** (2250), 119–123.

LEIBOVICH, S. 1977 Convective instability of stably stratified water in the ocean. *J. Fluid Mech.* **82** (3), 561–581.

LEIBOVICH, S. 1983 The form and dynamics of Langmuir circulations. *Annu. Rev. Fluid Mech.* **15** (1), 391–427.

LI, M. & GARRETT, C. 1997 Mixed layer deepening due to Langmuir circulation. *J. Phys. Oceanogr.* **27** (1), 121–132.

LI, Q. & BOU-ZEID, E. 2019 Contrasts between momentum and scalar transport over very rough surfaces. *J. Fluid Mech.* **880**, 32–58.

LUHAR, M., COUTU, S., INFANTES, E., FOX, S. & NEPF, H. 2010 Wave-induced velocities inside a model seagrass bed. *J. Geophys. Res.* **115**, C12005.

LUHAR, M., INFANTES, E., ORFILA, A., TERRADOS, J. & NEPF, H.M. 2013 Field observations of wave-induced streaming through a submerged seagrass (Posidonia oceanica) meadow. *J. Geophys. Res.* **118** (4), 1955–1968.

MCWILLIAMS, J.C. 2023 Surface waves and currents in aquatic vegetation. *J. Fluid Mech.* **958**, A14.

MCWILLIAMS, J.C. & SULLIVAN, P.P. 2000 Vertical mixing by Langmuir circulations. *Spill Sci. Technol. Bull.* **6** (3–4), 225–237.

McWilliams, J.C., Sullivan, P.P. & Moeng, C.-H. 1997 Langmuir turbulence in the ocean. *J. Fluid Mech.* **334**, 1–30.

Monismith, S., Alnajjar, M., Daly, M., Valle-Levinson, A., Juarez, B., Fagundes, M., Bell, T. & Woodson, C.B. 2022 Kelp forest drag coefficients derived from tidal flow data. *Estuar. Coast.* **45** (8), 2492–2503.

Nepf, H. & Ghisalberti, M. 2008 Flow and transport in channels with submerged vegetation. *Acta Geophys.* **56**, 753–777.

Nepf, H., Ghisalberti, M., White, B. & Murphy, E. 2007 Retention time and dispersion associated with submerged aquatic canopies. *Water Resour. Res.* **43** (4), W04422.

Nepf, H.M. 2012 Flow and transport in regions with aquatic vegetation. *Annu. Rev. Fluid Mech.* **44**, 123–142.

Pan, Y., Chamecki, M. & Isard, S.A. 2014 Large-eddy simulation of turbulence and particle dispersion inside the canopy roughness sublayer. *J. Fluid Mech.* **753**, 499–534.

Plew, D.R. 2011 Depth-averaged drag coefficient for modeling flow through suspended canopies. *ASCE J. Hydraul. Engng* **137** (2), 234–247.

Poggi, D., Porporato, A., Ridolfi, L., Albertson, J.D. & Katul, G.G. 2004 The effect of vegetation density on canopy sub-layer turbulence. *Boundary-Layer Meteorol.* **111**, 565–587.

Pope, S.B. 2000 *Turbulent Flows*. Cambridge University Press.

Qiao, F., Dai, D., Simpson, J. & Svendsen, H. 2009 Banded structure of drifting macroalgae. *Mar. Pollut. Bull.* **58** (12), 1792–1795.

Raupach, M. & Thom, A.S. 1981 Turbulence in and above plant canopies. *Annu. Rev. Fluid Mech.* **13** (1), 97–129.

Rominger, J.T. & Nepf, H.M. 2011 Flow adjustment and interior flow associated with a rectangular porous obstruction. *J. Fluid Mech.* **680**, 636–659.

Rosman, J.H., Denny, M.W., Zeller, R.B., Monismith, S.G. & Koseff, J.R. 2013 Interaction of waves and currents with kelp forests (Macrocystis pyrifera): insights from a dynamically scaled laboratory model. *Limnol. Oceanogr.* **58** (3), 790–802.

Rosman, J.H., Koseff, J.R., Monismith, S.G. & Grover, J. 2007 A field investigation into the effects of a kelp forest (Macrocystis pyrifera) on coastal hydrodynamics and transport. *J. Geophys. Res.* **112**, C02016.

Shaw, R.H. & Schumann, U. 1992 Large-eddy simulation of turbulent flow above and within a forest. *Boundary-Layer Meteorol.* **61** (1–2), 47–64.

Stevens, R.J.A.M., Graham, J. & Meneveau, C. 2014 A concurrent precursor inflow method for large eddy simulations and applications to finite length wind farms. *Renew. Energy* **68**, 46–50.

Suzuki, N. & Fox-Kemper, B. 2016 Understanding stokes forces in the wave-averaged equations. *J. Geophys. Res.* **121** (5), 3579–3596.

Teagle, H., Hawkins, S.J., Moore, P.J. & Smale, D.A. 2017 The role of kelp species as biogenic habitat formers in coastal marine ecosystems. *J. Expl Mar. Biol. Ecol.* **492**, 81–98.

Thom, A.S. 1971 Momentum absorption by vegetation. *Q. J. R. Meteorol. Soc.* **97** (414), 414–428.

Thorpe, S.A. 2004 Langmuir circulation. *Annu. Rev. Fluid Mech.* **36**, 55–79.

Troell, M., Joyce, A., Chopin, T., Neori, A., Buschmann, A.H. & Fang, J.-G. 2009 Ecological engineering in aquaculture–potential for integrated multi-trophic aquaculture (IMTA) in marine offshore systems. *Aquaculture* **297** (1–4), 1–9.

Tseung, H.L., Kikkert, G.A. & Plew, D. 2016 Hydrodynamics of suspended canopies with limited length and width. *Environ. Fluid Mech.* **16**, 145–166.

Utter, B.D. & Denny, M.W. 1996 Wave-induced forces on the giant kelp Macrocystis pyrifera (Agardh): field test of a computational model. *J. Expl. Biol.* **199** (12), 2645–2654.

Wyngaard, J.C. & Brost, R.A. 1984 Top-down and bottom-up diffusion of a scalar in the convective boundary layer. *J. Atmos. Sci.* **41** (1), 102–112.

Wyngaard, J.C. & Weil, J.C. 1991 Transport asymmetry in skewed turbulence. *Phys. Fluids* **3** (1), 155–162.

Yan, C., McWilliams, J.C. & Chamecki, M. 2021 Generation of attached Langmuir circulations by a suspended macroalgal farm. *J. Fluid Mech.* **915**, A76.

Yan, C., McWilliams, J.C. & Chamecki, M. 2022 Overlapping boundary layers in coastal oceans. *J. Phys. Oceanogr.* **52** (4), 627–646.